Spatially dependent kinetics of helium in tungsten under fusion conditions

Journal of Nuclear Materials 535 (2020) 152104

Contents lists available at ScienceDirect

Journal of Nuclear Materials

journal homepage: www.elsevier.com/locate/jnucmat

Spatially dependent kinetics of helium in tungsten under fusion conditions

V. Shah , J.A.W. van Dommelen *, M.G.D. Geers

Mechanics of Materials, Department of Mechanical Engineering, Eindhoven University of Technology, Eindhoven, The Netherlands

HIGHLIGHTS

- Synergistic neutron and helium irradiation under a temperature gradient in W monoblock is simulated for longer time-scales.
- Pronounce formation of helium-vacancy based defects is observed in the sub-surface region of the monoblock.
- Mobility based influence of the helium clusters on the defect evolution and diffusion length scales is investigated.
- Extended diffusion of helium in the bulk monoblock is noticed.
- A measure of the stored energy is obtained from the defect concentration in the monoblock.

GRAPHICAL ABSTRACT

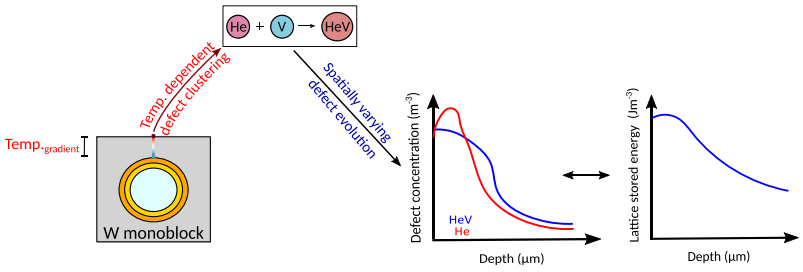

ARTICLE INFO

Article history:
Received 20 May 2019
Received in revised form
4 February 2020
Accepted 6 March 2020
Available online 12 March 2020

Keywords:
Cluster dynamics
Tungsten monoblock
Neutron irradiation
Helium implantation
Defect diffusion and accumulation
Helium resolution

ABSTRACT

Tungsten is the prime candidate material for divertor applications in future nuclear reactors (e.g. ITER and DEMO). In the present work, a spatially dependent cluster dynamics model is developed to investigate and understand the microstructure evolution of tungsten under low energy helium implantation and neutron irradiation varying over bulk length scales of millimetres and irradiation time scales of hours. The diffusion of helium, helium clusters and their trapping at neutron induced defects is simulated along the tungsten monoblock depth. The temperature gradient resulting from a steady state heat load of 10 MWm^{-2} along the monoblock depth is considered and its influence on the evolution of defects is discussed. The trapping of helium at vacancies and the associated formation of helium-vacancy clusters is found to be pronounced in the sub-surface layers. A significant influence of helium detrapping from grain boundaries and dislocations, along with its resolution from clusters, on the helium diffusion length scales is observed. Additionally, the effect of helium cluster mobility is investigated and overall lower retention in the monoblock bulk is observed through significant release of helium at the surface.

1. Introduction

Nuclear fusion is a potential sustainable energy source, owing to its near-zero carbon and combustion-free nature [1]. However, the realization of fusion as a commercial power source requires an

* Corresponding author.
E-mail address: j.a.w.v.dommelen@tue.nl (J.A.W. van Dommelen).

https://doi.org/10.1016/j.jnucmat.2020.152104

extensive lifetime of the future reactors and their components. Particularly, in the case of magnetic confinement based reactors (such as ITER and DEMO), the plasma facing components (PFC) in the divertor perform the vital function of extracting heat and helium ash from the plasma, and thus, their service lifetime is critical for an efficient and continuous operation of the reactor [2]. Furthermore, the design of the PFC (in case of ITER) is based on a monoblock geometry with bulk tungsten (W) bonded to an actively water cooled Cu alloy heat sink [3].

The choice of tungsten (W) as the candidate material for the PFC stems from its excellent high temperature properties such as the high melting temperature, high thermal conductivity, low sputtering yield and low tritium retention [4,5]. In service, the tungsten monoblocks will endure an extreme environment, characterized by intense neutron radiation peaking at 14 MeV energy ($\approx 10^{17}$-10^{18} neutrons $m^{-2}s^{-1}$), low energy hydrogen and helium gas fluxes (10^{22}-10^{24} ions $m^{-2}s^{-1}$) and high heat loads ($\approx$10 MWm^{-2} under steady state conditions) [6,7]. The high heat loads on the monoblock surface result in a high surface temperature ($\approx$1300°C), along with a steep temperature gradient in the bulk, thereby introducing high thermal stresses. Additionally, the defect generation by neutron irradiation, along with the diffusion and trapping of gas atoms, particularly helium, will result in defect accumulation in the monoblock bulk. The accumulated defects in combination with the temperature gradient will result in a multitude of thermo-mechanical degradation mechanisms, ultimately limiting the service lifetime and the structural integrity of the monoblocks. Therefore, understanding the evolution of tungsten monoblocks under the synergistic heat and particle loads at bulk length scales and time scales representative for reactor-like conditions is essential for accurately predicting the lifetime of the monoblocks.

The radiation effects of neutrons in metals are well understood and have been quite extensively studied for fission specific conditions. However in case of fusion conditions, the amount of data on neutron assisted radiation damage mechanisms is limited. In the bulk of the tungsten monoblocks, the fast fusion neutrons will primarily result in displacement damage in the form of lattice defects such as voids and dislocation loops [8]. In addition to the irradiation damage, the neutrons will also induce solid transmutation elements such as rhenium (*Re*) and osmium (*Os*) along with gaseous elements such as hydrogen (*H*) and helium (*He*) [9,10]. Furthermore, the accumulation of solid transmutants over time promotes solute segregation at grain boundaries (radiation induced segregation) and precipitate formation [11,12]. In terms of physical effects, these defects in the irradiated microstructure will contribute to hardening and loss of ductility, commonly referred to as neutron embrittlement. Thermodynamically speaking, the presence of radiation defects and dislocations in the microstructure implies a higher stored energy in the lattice, which in combination with high temperatures will lead to microstructure evolution by recovery, recrystallization and grain growth. In the past, several studies have reported the enhancement of recrystallization and grain growth kinetics in polycrystalline metals under irradiation [13–17], along with a decrease of the recrystallization temperature in the irradiated state compared to the unirradiated state [15]. For tungsten under fusion conditions, this implies that the occurrence of recrystallization and grain growth in the bulk may be inevitable as suggested by Mannheim et al. [18], where a multi-scale modelling approach was used to predict the microstructure evolution of tungsten under neutron loads.

The combined effects of plasma particles such as hydrogen isotopes, helium and the neutron induced defects have not been widely investigated, mainly due to the lack of an actual fast neutron source for testing and activation related material handling issues. To circumvent these drawbacks, a wide variety of studies have used high energy ion irradiation (self-ion or other ions) as a surrogate for neutrons, in combination with low energy hydrogen and helium plasma to mimic the synergistic loading conditions [19–21]. In some cases, high energy plasma ions are also used. However, due to the shallow penetration depth of ions, pre-dominantly surface evolution phenomena such as bubble formation, blister formation, micro-cracking, and nano-fuzz formation have been observed.

Furthermore, considering the irradiation effects in the bulk, the behaviour of helium in tungsten is more critical as compared to the hydrogen isotopes, owing to its chemical inert nature (unlike hydrogen isotopes), low solubility, high mobility and capability of forming bubbles, which can further act as trapping sites for hydrogen isotopes, thereby increasing their retention [21–24]. In tungsten, the trapping of helium atoms at lattice defects such as vacancies is reported to be energetically favourable, thereby resulting in the formation of helium-vacancy clusters [25]. These clusters develop into larger bubbles and platelets by trapping mobile helium atoms or vacancies. The interaction between the helium atoms is attractive in nature, leading to the formation of helium clusters [26]. The mobility of such helium clusters has been analysed extensively, and is dependent on the size of the cluster, i.e. the number of helium atoms inside the cluster [27–30]. However, the most salient feature of the helium clusters is their tendency to agglomerate together and to transform into a helium-vacancy cluster by ejecting a self-interstitial (SIA) atom, thereby acting as a source of defects in addition to the neutrons. Such a mechanism is known as a self-trapping event and its existence was first experimentally observed in tungsten by Nicholson and Walls [31]. Analogously, the growth of the helium-vacancy based clusters (helium bubbles) by ejection of a Frenkel-pair can also occur and is termed as trap-mutation or loop-punching (in the case when more than one SIA atoms are ejected together in the form of a dislocation loop). For tungsten, the validity of trap-mutation events has been verified in the experimental work of El Keriem et al. [25] and Iwakiri et al. [32] and in the MD simulations of Henriksson et al. [33]. Additionally, pronounced trapping of helium at microstructural sinks such as grain boundaries, dislocations and the sequential formation of helium bubbles have been observed experimentally in several metals including tungsten [34–37].

The implications of bubble formation along with other defects in the microstructure can be detrimental as they may lower the thermal conductivity [38], thereby raising the temperature gradient over the monoblock and the stresses induced, which may again promote recrystallization. However, the effect of bubble formation on recrystallization kinetics under fusion conditions are still unclear.

A number of studies in the past have reported the pinning of grain boundaries by gas bubbles [39–41] and recently, Guo et al. [42] have reported retardation of recrystallization following helium ion irradiation in tungsten. Yet, extrapolating the results from ion based irradiation studies to neutron based conditions can be erroneous and more experimental studies within this context are required. The evolution of the grain size by recrystallization and grain growth will also have an important consequence on the evolution of helium bubbles through the depth, as larger grain sizes, i.e. lower grain boundary density will result in lower trapping sites for helium, thereby leading to an increase of the diffusion length scales of helium. In this context, several studies have proposed the use of nano-crystalline and ultra-fine grained tungsten to mediate the effect of helium bubble formation and growth in the grain matrix [37,43,44]. Nevertheless, the lifetime of such a fine grain structure under fusion conditions is questionable (relatively large grains along with a change in the grain boundary character have been reported due to recrystallization in the bulk of monoblocks following high heat flux exposure by Shah et al. [45]) and the

formation of helium bubbles at grain boundaries in combination with high temperatures can assist in high temperature helium embrittlement [46–48].

The microstructural defect evolution under irradiation is a multi-scale phenomenon in time and space and its long term evolution can be modelled using mesoscopic models such as object kinetic Monte-Carlo (OKMC) or cluster dynamics (CD, also known as mean field rate theory) [49]. The pre-requisite for both approaches is adequate input regarding the production rate of defects, and their energetics and mobility. The fundamental difference between the approaches relates to the solution method for the defect evolution. In a CD based approach, the defects evolve deterministically, whereas in an OKMC based approach, the defects evolve stochastically. An extensive comparison between the two approaches is provided by Stoller et al. [50]. One of the main limitations of the OKMC approach is the limited simulation volume, of the order of few hundred nanometers, whereas on the other hand, theoretically, cluster dynamics has no limitations on the cluster size and can be used to simulate large defect clusters. However, for the CD approach, the deterministic solution procedure along with large defect clusters is computationally challenging and expensive. In this context, several different schemes ranging from averaging schemes to the use of hybrid solution procedures have been proposed to reduce the computational cost associated with the CD approach [51–54].

The dynamics of helium in the presence of irradiation damage in tungsten has been investigated using the OKMC approach as well as the CD approach [27,55–58]. In the work of Faney et al. [27], the formation of nano-tendrils under helium exposure in tungsten was simulated using the CD approach and a reasonable agreement between experimental and numerical predictions of the tendril geometry was obtained. Furthermore, a good match between experimental helium thermal desorption spectra [59] and numerical predictions were reported, thereby demonstrating the ability of the CD approach to reproduce the experimental observations. Recently, Zhao et al. [58] investigated the influence of grain size on He retention using a CD approach and reported lower He retentions in coarse grained tungsten. However, the applicability of these studies is valid for lower ion fluences and considering the practical application of tungsten monoblocks in fusion reactors, the dynamics of helium in conjunction with neutron irradiation at higher ion fluences has not been studied.

The aim of this paper is to describe the microstructure evolution of tungsten in terms of defect evolution under synergistic neutron irradiation and helium implantation conditions at larger length and longer time-scales. At atomic length scales, the interaction of the radiation induced defects with helium atoms are accounted for and these microstructural level interactions are linked to the mesoscopic length scales by considering a spatial dependency through diffusion of defects along the monoblock depth. The effect of a temperature gradient along the monoblock depth on the defect evolution is discussed. Moreover, the mobility of helium based clusters on the overall defect evolution and total helium retention is analysed. Additionally, the spatially varying defect concentrations predicted by the model are scrutinized in terms of the spatially varying lattice stored energy, providing a measure for the driving force for recrystallization and grain growth in the monoblock bulk. Finally, the importance of helium resolution and sink detrapping based mechanisms on the helium diffusion length scales for longer irradiation time-scales ($\approx$ hours) is highlighted.

[1] The term defects in this paper is used to represent both isolated defects (point defects) as well as their clusters.

2. Numerical model

The evolution of irradiation induced lattice defects,[1] along with their interaction with the plasma implanted helium ions is modelled using a cluster dynamics approach, based on the work of Li et al. [60], Faney et al. [27] and Jourdan et al. [53]. The cluster dynamics approach is an extension of the classical kinetic rate theory (also known as mean field rate theory [61–64]), in which the temporal evolution of each defect concentration is described by means of a first order non-linear ordinary differential equation (ODE), accounting for the production, annihilation and interaction with other defects. To account for the spatial variation of mobile defects, an additional term describing the diffusion of defects in space is introduced, thereby resulting in a partial differential equation (PDE). Generally speaking, the spatially resolved cluster dynamics approach can be perceived as a system of coupled reaction-diffusion equations, and can be expressed generically in terms of a Master Equation (ME), having the form:

$$\frac{\partial C_{\theta_n}}{\partial t} = G_{\theta_n} + \frac{\partial}{\partial x}\left(D_{\theta_n}\frac{\partial C_{\theta_n}}{\partial x}\right) + \sum_{\theta'_n}[J(\theta'_n,\theta_n) - J(\theta_n,\theta'_n)] - L_{\theta_n}, \quad (1)$$

where, θ_n denotes the defect type (mobile as well as immobile), C_{θ_n} the volumetric concentration of the defect at a specific location and time, and G_{θ_n} the production rate of the defect, also known as the source term. The term containing the second order spatial derivative accounts for the diffusion in one dimension of the mobile defect, whereas the terms $J(\theta'_n,\theta_n)$ and $J(\theta_n,\theta'_n)$ are fluxes due to the growth and shrinkage of the defect by the absorption or emission of mobile defects (see Fig. 1). The term L_{θ_n} accounts for the trapping of mobile defects at microstructural sinks. Details regarding the nature of the defects and the associated interaction rules are summarized in the following section and the master equations for all defects are detailed in Appendix A.1.

2.1. Defect evolution process

As discussed earlier, the primary effect of neutron irradiation in metals is generation of lattice defects, with production of nano-scale loops and clusters during the initial stage of a collision cascade, i.e. the heat spike governed displacement. However, the majority of these defects are recovered during the cooling stage of the cascade. Furthermore, the self-interstitials tend to accumulate, ultimately leading to the formation of prismatic self-interstitial dislocation loops. On the other hand, the surviving vacancies can assemble to produce three different kinds of defect types, i.e. prismatic vacancy dislocation loops, planar vacancy clusters and voids, predominantly governed by the number of accumulated vacancies and the irradiation temperature [65]. Moreover, the solute/gas atoms produced by transmutation or implantation can get trapped at the neutron induced defects, thereby forming mixed defect complexes. In tungsten, conventional TEM and in-situ TEM based techniques have been widely used to probe the type of defects produced and commonly, defects such as vacancy clusters, voids, prismatic dislocation loops, helium bubbles (helium-vacancy clusters) have been observed by literature studies following neutron [66,67] and ion irradiation [43,68–72]. Additionally, information about the nature of the dislocation loops can be availed through inside-outside contrast mode in TEM [73], and both vacancy type defects [69,74] as well as self-interstitial type defects [71,75] have been observed. Thus, following the experimental observations in tungsten, the type of defects accounted for in the present model are vacancies (V), self-interstitial atoms (SIAs, symbol: I), helium atoms (He) and their clusters (V_m, I_n, He_n with m

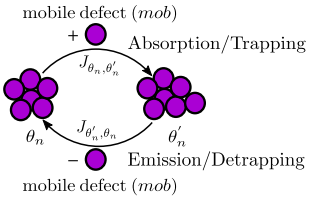

Fig. 1. Schematic representation of the growth of defect type θ_n and shrinkage of defect type θ'_n, with flux J_{θ_n,θ'_n} describing the transition between the defects θ and θ'.

and n ranging from 2 to the maximum number of defect species in the cluster, i.e. $M_V/N_I/N_{He}$) along with the mixed helium-vacancy clusters (He_nV_m, with n and m ranging from 1 to the maximum number of defect species inside the cluster, i.e. N_{He} and M_V). Furthermore, considering the temperature range of interest (i.e. 600-1500 K) in the present work, the formation of prismatic vacancy dislocation loops is ignored due to their relatively low stability and tendency to transform into voids due to the increased vacancy mobility at higher temperatures [65].

Vacancies (V), SIAs (I), di-interstitials (I_2) and helium atoms (He) are treated as mobile species. Several literature studies [27,29,76] have reported small helium based clusters, i.e. He_n with $2 < n \leq 6$ to be mobile within the time-scales of molecular dynamics simulations (MD-simulations). Thus, smaller helium based clusters (here limited to $n = 5$) are also treated as mobile species in the present work. Within the context of mixed He_nV_m clusters, Perez et al. [77] have demonstrated through accelerated molecular dynamics (AMD, time-scales $\approx$milli-seconds) that the mobility of mixed He_nV_m clusters is greatly dependent on the number of helium atoms contained within the cluster and resembles the case of trap-mutation assisted diffusion. However, the temperature dependent diffusivity of such clusters is not well defined and in general, the diffusivity is orders of magnitude smaller compared to small He_n clusters. It is therefore assumed that the effect of the mobility of He_n clusters on the overall defect distribution and retention is more significant, than the effect of mobile mixed He_nV_m clusters. Hence, all the mixed He_nV_m clusters are treated as immobile species further on. For the case of SIA loops (I_n), Jin et al. [78] observed a significant influence of mobile SIA loops (I_n, with n ranging between 1 and 6) on the overall defect size distribution. However, the work from Jin et al. [78] does not account for the effect of solute atoms on the overall defect size distribution such as the *He* atoms, which is expected to have a major effect on the evolution of the defect size distribution by trapping at V. A similar conclusion with respect to the role of mixed (He_nV_m) clusters on the suppression of the SIA loop migration is also reported by Watanabe et al. [75]. Hence, the larger SIA loops (I_n, $n > 2$) as well as vacancy based clusters (V_m, $m > 1$) are considered immobile in the present model.

The production of defects due to neutron irradiation following the time scales of molecular dynamic (MD) simulations is used as input. The corresponding source term accounts for the cascade and sub-cascade processes along with the associated defect recombinations and introduces defects in isolated and clustered form. Considering ITER-like conditions and the tungsten monoblock geometry of the plasma facing components, the helium production is here modelled using a surface source. The losses of the mobile defects at microstructural sinks, in the form of grain boundaries and dislocations are accounted for. The microstructural sinks are incorporated using a mean field approach, where the loss of mobile defects is governed by the sink strength. For mobile defects V, I, I_2, the microstructural sinks are assumed to be perfect, i.e. no emission of such defects is allowed, whereas for the solute atoms, i.e. *He*, detrapping of *He* atoms from the sinks is allowed. To account for the displacive effects of the neutrons on He_n clusters, mixed He_nV_m clusters and *He* atoms at the sinks, the resolution of *He* atoms into the matrix by direct collision with neutrons is accounted for in the present model. The growth of the vacancy based clusters (V_m) can only occur by absorption of V, whereas the vacancy based clusters (V_m) can shrink by emitting V or by absorbing mobile I and I_2. Additionally, the mobile *He* atoms can be trapped by the mobile V, resulting in the formation of a *HeV* cluster.

Self-interstitial loops can grow by absorbing mobile I or I_2, and conversely, shrink by emitting mobile I or I_2. In addition, the SIA loops can also shrink by absorbing a mobile V. A weak interaction of mobile SIAs by helium based clusters (He_n) has been observed by Watanabe et al. [75] and Fu and Willaime [79], which was incorporated in the cluster dynamics work of Li et al. [57,60] and Marian and Hoang [80]. However, in preliminary simulations, the influence of helium bound SIA clusters (He_nI) on the overall defect distribution was found to be negligible, with relatively low concentrations (similar magnitude as reported by Li et al. [57,60]). Hence, the interaction between the helium based clusters (He_n) and SIAs (I) is ignored here. A similar conclusion with respect to the importance of such a clustering reaction has also been drawn by Gao and Ghoniem [81]. As the interaction between helium atoms is attractive in nature, the growth and shrinkage of helium based clusters (He_n) by absorption or emission of mobile *He* atoms is allowed. Furthermore, literature studies addressing the minimum size of helium based clusters for occurrence of a self-trapping event (i.e. the formation of a helium-vacancy cluster (*HeV*) accompanied by the simultaneous formation of a SIA) are not conclusive. Thus, in the present work, the occurrence of self-trapping event for He_n clusters with more than 6 *He* atoms is accounted for, based on the density functional theory (DFT) simulations of Boisse et al. [82,83].

Mixed He_nV_m clusters are allowed to grow by absorbing/trapping the freely migrating *He* atoms and V, and conversely, the emission of *He* atoms or detrapping of V from mixed He_nV_m clusters is permitted. Moreover, the mixed He_nV_m clusters are also allowed to shrink by trapping mobile I and I_2. The trap-mutation phenomenon for the mixed He_nV_m clusters, i.e. the growth of the He_nV_m clusters by ejection of SIAs, is known to be dependent on the ratio of the number of the *He* atoms and the number of V in the cluster, i.e. the n/m ratio. Within this context, the trap-mutation phenomenon for the mixed He_nV_m clusters in the present model is considered to be dependent on the n/m ratio, based on the work of Boisse et al. [82,83]. For mobile small He_n based clusters ($2 \leq n \leq 5$), only absorption based clustering reactions are accounted for, i.e. the mobile/immobile helium clusters (He_n) can grow by absorbing the mobile helium clusters, but emission of a particular mobile helium cluster from a larger helium cluster is not permitted. This restriction is applied due to the lack of adequate information on the binding energies between the helium-helium clusters. Similarly, the mixed He_nV_m clusters are allowed to grow by trapping mobile He_n clusters, but their shrinkage by detrapping of mobile He_n clusters is not permitted. The nucleation of mixed He_nV_m clusters by trapping of mobile He_n clusters by immobile V_m based clusters is also accounted for.

In tungsten (W), the trapping of mobile defects V, I, and He_n based clusters ($1 \leq n \leq 3$) by processing induced impurities such as carbon (*C*), molybdenum (*Mo*), and transmutation products, i.e. rhenium (*Re*), are well known [84]. Considering the strong interaction of carbon with the point defects, specifically vacancies (V), the formation of carbon-vacancy complexes can lower the *He-V* based clustering, thereby preventing the nucleation and growth of helium bubbles [85,86]. Similarly, the trapping of helium by carbon can also inhibit the formation of helium bubbles [85]. Furthermore, taking into account the magnitude of the trapping energy between the impurities (such as *C, Mo*) and other defects (V, *He*), in addition

to the relatively low concentration of the impurities in the fusion relevant tungsten grade, it can be argued that the interaction reactions between the helium and neutron induced defects may dominate the overall defect distribution. Thus, for the sake of simplicity, the presence of impurities (processing as well as transmutation products) as traps for mobile defects is neglected in the present work. Nevertheless, conclusive statements regarding the role of impurities (specifically carbon (10 appm) and molybdenum (300 appm) [87]) as trapping sites under fusion relevant conditions demand further detailed investigations. Appendix A.2 summarizes the complete set of defect interaction reactions accounted for in the current model along with their associated rate coefficients.

2.2. Rate coefficients

The interaction reactions between defects are described by means of rate coefficients (Appendix A.2) with "+" denoting a absorption/trapping based reaction rate and " − " representing an emission/detrapping based reaction rate. The absorption flux can be described in terms of an absorption/trapping reaction rate as $J_{\theta_n,\theta'_n} = k^{+}_{\theta_n,mob} C_{\theta_n} C_{mob}$ (with C_{mob} representing the concentration of the mobile defect), whereas the emission/detrapping flux in terms of a emission/detrapping reaction rate is given as $J_{\theta'_n,\theta_n} = k^{-}_{\theta'_n} C_{\theta'_n}$, see Fig. 1. The absorption/trapping based rate coefficient is derived based on the diffusion-limited theory approximation [88] and is governed purely by the capture radii of the reacting defects and their diffusivity. The emission/detrapping rate coefficient is similar to the absorption/trapping rate coefficient with an additional thermodynamic parameter called the binding energy, accounting for the free energy increase associated with the emission or detrapping of mobile defect from the defect clusters.

For spherical clusters such as V_m, He_n and mixed He_nV_m based clusters, with an isotropic diffusion of mobile defects (3-D motion of defects), the absorption/trapping rate is given by:

$$k^{+}_{\theta_n,mob} = 4\pi r_{\theta_n} D_{mob} Z^{\theta_n}_{mob}, \tag{2}$$

where, r_{θ_n} is the capture radius, commonly defined as the sum of the radii of the reacting defects with a constant interaction distance, D_{mob} is the diffusivity of the mobile defects and $Z^{\theta_n}_{mob}$ is the capture efficiency factor accounting for the preferential absorption by a particular defect type θ_n, depending on their strain field. In case of V_m, He_n and mixed He_nV_m clusters, the capture efficiency factor is of the order unity. Further, the detrapping rate is defined as:

$$k^{-}_{\theta'_n} = \frac{1}{\Omega}\, k^{+}_{\theta_n,mob} \exp\left[\frac{-E^{b}_{(\theta_n - mob)}}{k_B T}\right], \tag{3}$$

with $E^{b}_{(\theta_n - mob)}$ representing the binding energy between the defect θ_n and the mobile defect, k_B is the Boltzmann constant and T is the temperature.

For pure vacancy based cluster interactions, the capture radius is given as $r_{V_m} = (3m\Omega/4\pi)^{(1/3)} + r_V$, in which m represents the cluster size, Ω is the atomic volume, and r_V is the capture radius of vacancies. The capture radius of V is defined as half the distance of the vacancy to its nearest neighbour, which in terms of the tungsten lattice parameter (a_0) is given as $r_V = (\sqrt{3}\, a_0\, /4)$. Similarly, for pure helium based cluster interactions, the capture radius is given as $r_{He_n} = (3n\Omega/4\pi)^{(1/3)} + r_{He}$, with r_{He} defining the capture radius of a single helium atom, approximated as 95% of the tungsten lattice parameter [27]. For the mixed He_nV_m cluster based interactions, the capture radii are only governed by the number of V in the clusters and hence are evaluated in a similar manner as for V_m clusters [27,57,60,76]. In the special case of the annihilation reaction between the mobile V and mobile I, a larger capture radius equal to 0.465 nm is used [57,60].

The self-interstitial loops (dislocation loops) are assumed to be non-spherical, i.e. of toroidal shape [57,60] and the absorption/trapping rate for a mobile defect is given as:

$$k^{+}_{I_n,mob} = 2\pi r_{I_n} D_{mob} Z^{I_n}_{mob}, \tag{4}$$

where, r_{I_n} is the loop radius, given by $r_{I_n} = \sqrt{(n\Omega/\pi b)}$, with b the Burgers vector of the loop. Furthermore, the capture efficiency factor $Z^{I_n}_{mob}$ is based on the elastic defect-dislocation interaction, in addition to the toroidal shape of the loop and is given as $Z^{I_n}_{mob} = Z^{D}_{mob} \max\left\{\frac{2\pi}{\ln(8r_{I_n}/2b)}, 1\right\}$, with Z^{D}_{mob} representing the capture efficiency factor accounting for the preferential absorption of the mobile defect by the dislocation lines. For SIA based defects, Z^{D}_{mob} deviates from unity. The emission or detrapping rate of mobile defects from the loops is obtained from the trapping rate, in a similar fashion as mentioned before.

The rate coefficients accounting for the absorption/trapping of mobile defects at the microstructural sinks such as dislocations and grain boundaries, are determined based on the sink strength for the defects. For the dislocations, the absorption/trapping rate (k^{+}_{D+mob}) is dependent on the network dislocation line density ρ_n, the diffusivity of the mobile defect D_{mob} and the capture efficiency factor Z^{D}_{mob}, together defined as $k^{+}_{D+mob} = \rho_n D_{mob} Z^{D}_{mob}$.

For grain boundaries, the absorption/trapping rate (k^{+}_{GB+mob}) of a mobile defect is dependent on the cumulative sink-strength of the defect clusters inside the grain, including the dislocations and the diffusivity of the mobile defect D_{mob}. The expression for the grain boundary sink strength S^{sk}_{mob} is based on the cellular sink strength model of Bullough et al. [89] and takes the form:

$$S^{sk}_{mob} = S^{m}_{mob}\left[\frac{\sqrt{S^{m}_{mob}}d}{2}\coth\frac{\sqrt{S^{m}_{mob}}d}{2} - 1\right] \times \left[1 + \frac{S^{m}_{mob}d^2}{12} - \frac{\sqrt{S^{m}_{mob}}d}{2}\coth\frac{\sqrt{S^{m}_{mob}}d}{2}\right]^{-1} \tag{5}$$

where, S^{m}_{mob} is the cumulative sink strength inside the grain for the considered mobile defect and d is the grain size. Thereby, the absorption/trapping rate is expressed as $k^{+}_{GB+mob} = S^{sk}_{mob} D_{mob}$. The detailed set of rate coefficients for different interaction reactions are listed in Appendix A.3.

2.3. Binding energy

The binding energy between the defects is an essential input parameter governing the growth and shrinkage dynamics of defects. Thus, determining an accurate the binding energy is essential, in order to predict the correct evolution behaviour of defects. For the case of pure vacancy defects, i.e. clustering of vacancies, datasets based on the DFT simulations of Becquart and Domain [55], Becquart et al. [84] and MD simulations of Ahlgren et al. [90] are available, with the stability of the di-vacancy clusters being debatable. In the current work, the di-vacancy clusters are considered as stable clusters (positive binding energy) and the data

set from the MD simulations of Ahlgren et al. [90] is used to describe the energetics of vacancy clustering. For smaller vacancy cluster sizes (V_m, $m \leq 2$), the results from MD simulations are used, whereas for larger cluster sizes, the binding energies are derived from the capillary law approximation [84]. Conversely, for the case of pure helium defects, the DFT based values from the work of Becquart et al. [84] are adopted to retrieve the binding energy between two helium atoms, with the use of the capillary approximation for larger clusters. For the case of pure SIA defects, the capillary law approximation with the DFT based SIA formation energy [91] and di-interstitial binding energy [84] is used, which is in good agreement with the DFT results from Becquart et al. [84] and calculations based on the elasticity theory of dislocations from Fikar and Schäublin [92].

To describe SIA loop-growth by vacancy emission, the binding between mixed I_n loops and mobile V is described by means of the capillary approximation, based on the work of Li et al. [57,60]. Furthermore, for the mixed He_nV_m clusters, the binding energy of V/He atoms with a mixed He_nV_m cluster is dependent on the n/m ratio. In the present paper, this binding energy is identified on the basis of the DFT results of Boisse et al. [82,83], limited to $n \leq 30$ and $m \leq 4$. The binding energies for larger mixed He_nV_m clusters are determined through extrapolation, in similarity with the work of Li et al. [60]. It is worthwhile to mention that for binding of V/He atoms with the mixed He_nV_m clusters, the differences between the MD based predictions [93] and DFT based predictions are minor [82,83].

Similarly, the binding energies for the self-trapping and trap-mutation events are identified on the basis of the DFT results of Boisse et al. [82]. The binding energy for the self-trapping event is a function of the number of the He atoms inside the cluster (He_n), and is energetically favourable for $n \geq 6$. For trap-mutation based events, i.e. for mixed He_nV_m clusters, the binding energy depends on the n/m ratio and is energetically favourable for an n/m ratio exceeding 8 (sensitive to the size of the mixed He_nV_m cluster). In principle, the binding energy between the I and He_nV_m required to quantify the trap-mutation can be determined from the Frenkel pair formation energy and the binding energy between the vacancies and He_nV_m clusters, and does not require a mathematical function.

Fig. 2a schematically shows the binding energy results as a function of the n/m ratio, along with the activation energy for the trap-mutation events obtained from the DFT results of Boisse et al. [82,83], whereas Fig. 2b graphically shows the activation energy for the self-trapping events. The detailed set of binding energy relations between the defects and the related defect parameters can be found in Appendix A.4.

2.4. Migration energy of defects

Similar to the binding energies, the migration energies of defects are an essential input parameter in the cluster dynamics model, describing the diffusivity of defects. As mentioned earlier, in the present model, vacancies (V), helium (He) and helium based clusters (He_n; $1 < n \leq 5$) are assumed to be mobile, in a three dimensional space. Additionally, the small SIA based clusters, i.e. up to size 2 are assumed to be mobile, based on the work of Li et al. [60], with a three dimensional motion. Furthermore, for bcc metals (specifically tungsten), Amino et al. [94] have shown through their OKMC simulations that the SIAs tend to undergo one dimensional motion, thereby enhancing the SIA-V based recombination due to highly spatially correlated interaction between these defects. At the same instance, it has also been shown that for homogeneously distributed sinks such as the SIAs and the impurities, the reaction between the SIAs−SIAs and SIAs-impurities can be lower as these interactions are not strongly correlated [94]. The consequence of these changes in the reaction rate between the defects in presence of the one dimensional motion of SIAs is the lowered nucleation rate of SIA loops. However, the extent of the one dimensional SIA motion on the defect evolution in the presence of helium atoms has not been depicted in literature. For example, the enhanced SIA-V recombination probability due to one dimensional SIA motion may be lowered due to the higher affinity of helium atoms towards vacancies, i.e. formation of He_nV_m clusters, which are expected to have negligible influence on the nucleation rate of SIA loops. Hence, based on this reasoning, the one dimensional motion of the SIA based defects is ignored in the model.

In the case of V, I and He, the migration energy based on the ab-initio simulations of Becquart et al. [84] is adopted, whereas for I_2, the migration energy resulting from the molecular dynamics simulations of Faney and Wirth [76] and Faney et al. [27] is used. Note that for I, I_2 and He, the difference between the ab-initio and MD based migration energies is small. The ab-initio based vacancy migration energy lies within the experimentally measured range [95,96] as compared to the ones obtained through MD simulations. For the case of small He_n based clusters, several studies [27–30,76,84] have investigated and reported their diffusion properties. Theoretically, it can be assumed that the migration barrier for helium clusters will increase for a larger number of helium species inside the cluster. A similar trend is also observed in the work of Becquart et al. [84], Faney and Wirth [76] and Faney et al. [27]. It is important to remind that in the work of Becquart et al. [84], He_n clusters up to size 50 were assumed to be mobile to reproduce the experimental results of lower helium concentration, whereas in the work of Faney et al. [27] and Faney and Wirth [76], within the MD time-scales, clusters with a size up to 5 were found to be mobile. Thus, considering the validity of the MD based results, the migration energy of helium based clusters from the work of Faney et al. [27] is exploited in the current model. Furthermore, the migration energy of the defects is used to extract the temperature dependent diffusivity through an Arrhenius type relation, i.e. $D_\theta = D_\theta^0 \exp(-E_\theta^m/k_BT)$, where θ is the defect type, D_θ represents the diffusivity, D_θ^0 is the pre-exponential factor, E_θ^m is the migration energy. The migration energy and the associated pre-exponential factor of the mobile defects (determined using MD simulations), used to calculate the temperature dependent diffusivity are summarized in Appendix A.5.

2.5. Network dislocation evolution

In the presence of irradiation, the production of lattice damage in terms of point defects, in combination with high temperatures will assist in climb based processes, thereby evolving the network dislocation density. In the present model, the evolution of the network dislocation density is based on the work of Stoller and Odette [97] and Stoller [98], and is expressed as:

$$\frac{d\rho_n}{dt} = 2\pi\nu_{cl}S_{BH} - \rho_n\tau_{cl}^{-1}, \tag{6}$$

where, the first term on the right hand side represents the climb based dislocation source, also known as the Bardeen-Heering source (BH) and the second term accounts for mutual annihilation of dislocations by climb. The BH source is based on the growth (increase in line length) of a pinned dislocation segment by climb, i.e. absorption/emission of vacancies/SIAs, ultimately leading to a dislocation loop within the climb plane. The generation rate of a dislocation loop by a BH source is governed by the climb velocity v_{cl} of the dislocation segment and is a function of the point defect saturation, internal stress and temperature. The climb velocity is

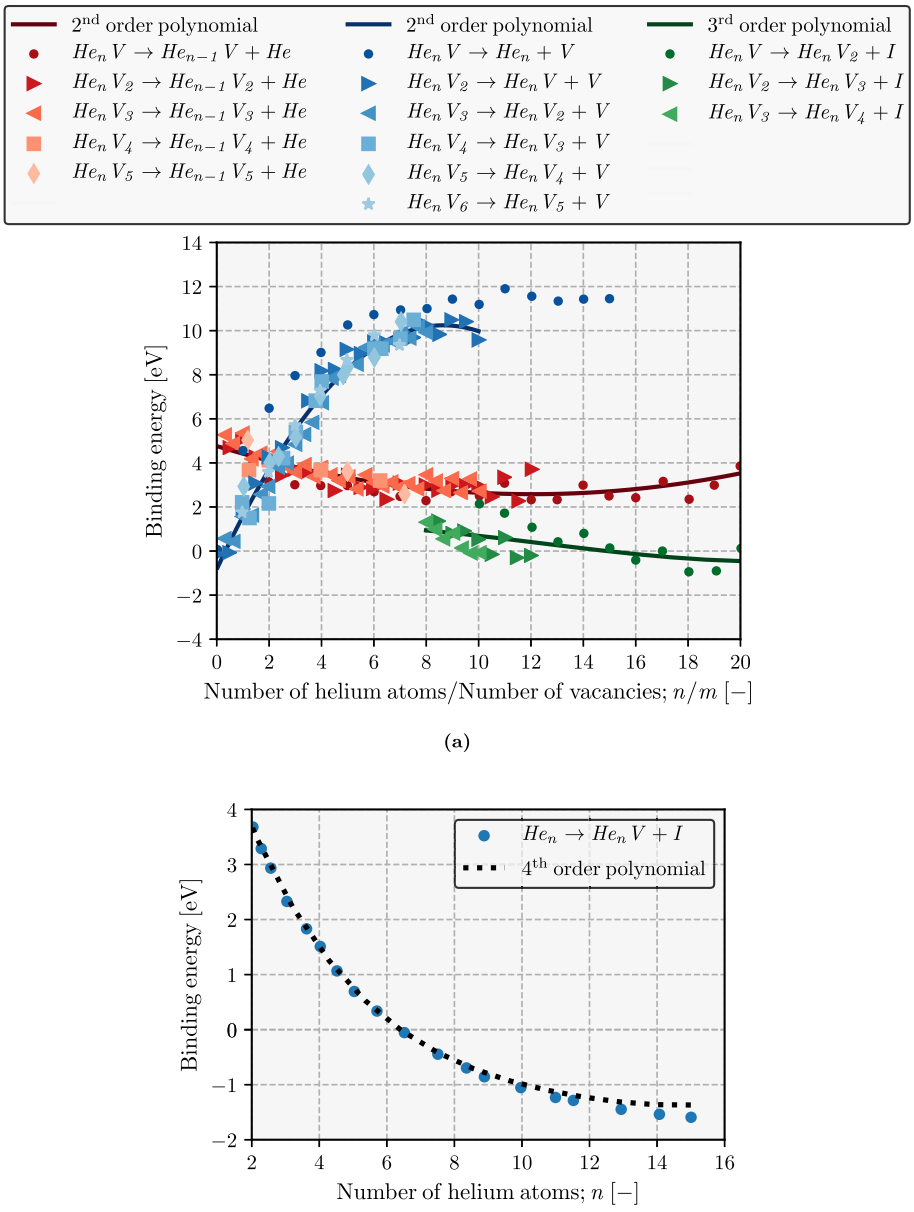

Fig. 2. **(a)** Binding energy of helium atoms (*He*) and vacancies (*V*) with a mixed He_nV_m cluster, and the trap-mutation energy as a function of the *n*/*m* ratio. **(b)** Self-trapping energy for a pure helium based cluster as a function of the number of helium atoms inside the cluster. Markers represent the results from DFT simulations [82,83], whereas the solid line represents the identified parametric relation. (For interpretation of the references to colour in this figure legend, the reader is referred to the web version of this article.)

expressed as:

$$v_{cl} = \frac{2\pi}{b \ln(r_o/r_i)} \left[Z_I^D D_I C_I + 2 Z_{I_2}^D D_{I_2} C_{I_2} - Z_V^D D_V (C_V - C_V^n) \right], \tag{7}$$

where, b is the magnitude of the Burgers vector of the dislocation segment, r_o/r_i represents the dislocation geometry factor, i.e. the ratio between the outer radius of the cylindrical cell around the dislocation and the dislocation core radius. Theoretically, the dislocation geometry factor is inversely proportional to the square root of the dislocation density ($1/\sqrt{\rho_n}$) [98,99] but here is approximated as 2π, based on the evaluation of the dislocation geometry factor with an upper bound dislocation density of 10^{16} m^{-2} and a core radius of $3b$. The parameters Z_{mob}^D, D_{mob} and C_{mob} represent the dislocation capture efficiency, diffusivity and concentration of the mobile SIAs, di-interstitials and vacancies. The parameter C_V^n denotes the concentration of the vacancies in equilibrium with the dislocation segment and is expressed as $C_V^n = C_V^{eq} \exp(\sigma\Omega/k_B T)$, where the parameter σ is dependent on the pinned dislocation density (ρ_p), and given by $\sigma = 0.4\mu b\sqrt{\rho_p}$. The BH source density (S_{BH}) is considered to be temperature independent and depends on the pinned dislocation density ρ_p, expressed as $S_{BH} = (\rho_p/3)^{1.5}$.

The rate of climb assisted mutual annihilation of dislocations is dependent on the mean lifetime τ_{cl} of the dislocation prior to annihilation, i.e. the duration during which the dislocation can climb before annihilating with another dislocation of opposite sign. The lifetime is expressed in terms of the average climb distance d_{cl}

and the climb velocity v_{cl} as $\tau_{cl} = d_{cl}/v_{cl}$, with the average climb distance d_{cl} defined as $d_{cl} = (\pi\rho_n)^{-1/2}$.

In the current model, the increase in the network dislocation density by unfaulting of SIA loops is not considered. This assumption is based on the fact, that the size of the modelled SIA loops in the model is not large enough to trigger a loop intersection based process, thereby lowering the probability of loop incorporation into the dislocation network to a bare minimum.

2.6. Evolution of helium at microstructural sinks

In the present model, the concentration of helium atoms at the microstructural sinks such as grain boundaries and dislocations is accounted for, based on the work of Jourdan et al. [53]. Furthermore, Jourdan et al. [53] have categorized for sub-classes of microstructural sinks, i.e. different types of grain boundaries and dislocations, driven by binding energy based criteria. However for the sake of simplicity, such a sub-classification of the microstructural sinks is not used here, consistent with the work of Zhao et al. [58].

In studies based on low fluences, i.e. smaller irradiation time scales (few seconds), the detrapping of helium atoms from the microstructural sinks is usually ignored under the assumption of unsaturated sinks [27,58,60]. However, under practical fusion conditions, i.e. irradiation time scales of hours, the saturation of the helium concentration at sinks will occur by balancing the accumulation and emission of helium atoms. Intrinsically in CD approaches, the microstructural sink strengths are treated as infinite sinks and do not account for saturation [50]. Thus, an additional reaction term representing the detrapping of helium atoms from microstructural sinks is incorporated into the microstructural sink strength term. Additionally, the resolution assisted emission of helium from microstructural sinks is also incorporated and the resulting equation representing the evolution of helium at the microstructural sinks is expressed as:

$$\frac{dC_{He}^{sink}}{dt} = S_{He}^{sink} D_{He} C_{He}^{matrix} + \sum_{n=2}^{5} n S_{He_n}^{sink} D_{He_n} C_{He_n}^{matrix} - \zeta_{sink,He}^{-} C_{He}^{sink} - \delta_{resol} C_{He}^{sink}, \tag{8}$$

where, C_{He}^{sink} is the concentration of helium atoms at the microstructural sinks, i.e. grain boundaries and dislocations, $C_{He_n}^{matrix}$ is the concentration of helium and helium-based clusters in the grain interior ($1 \leq n \leq 5$), and the parameter S_i^{sink} represents the microstructural sink strength for helium based clusters (in the case when the mobility of helium based clusters is not considered, the second term on the right hand side equals zero). The third term represents the detrapping of helium atoms from the sink and the rate coefficient is defined as $\zeta_{sink,He}^{-} = \nu_{He}\exp(-E_{sink,He}^{b}/k_B T)$, with ν_{He} defined as the vibrational frequency of helium in tungsten. The fourth term describes the resolution assisted emission of helium from the sinks and is explained in detail in the following section.

The rate coefficient $\zeta_{sink,He}^{-}$ describing the emission of helium atoms from the microstructural sinks depends purely on the binding (segregation) energy $E_{sink,He}^{b}$ between the sink and the helium atom. For dislocation type sinks, a binding energy of 1.53 eV (edge dislocations) obtained from the DFT based calculations of de Hosson et al. [100] is used.

In case of grain boundary type sinks, several studies [101–103] have investigated the influence of the grain boundary morphology on the helium segregation energy, with values ranging between 1.2 and 3.74 eV (discrepancies related to helium segregation energy at special grain boundaries exist in the literature). Accordingly, a lower bound value of 1.37 eV from the MD simulations of Zhou et al. [101] is adopted.

2.7. Dynamic resolution of helium

The synergistic effect of neutron assisted generation of defects and trapping of helium atoms at these defects was discussed earlier. However, another physical mechanism that can occur under the synergistic loads of neutrons and helium is known as the resolution mechanism [104–106]. As the name implies, the resolution mechanism refers to a process by which the *He* atoms present in the mixed He_nV_m clusters, He_n clusters and at the microstructural sinks are driven back into the matrix (grain interior) by irradiation. In fission based nuclear systems, the resolution mechanism is recognized as a driver for swelling phenomena owing to the higher fraction of atomically dispersed helium gas [104]. However for fusion conditions, i.e. at monoblock length scales, the higher fraction of helium atoms in the matrix and their diffusion, will result in a competing effect between the surface release of helium and penetration into the bulk. Furthermore, with respect to the nature of collisions, two different resolution mechanisms have been proposed in literature [104,105], i.e. resolution by direct neutron collision and resolution by collision cascades. In the present work, only the direct resolution of *He* atoms by neutrons is considered. The direct resolution parameter $\delta_{resol.}$ represents the probability per second that a collision of a neutron with *He* atoms in the clusters/sinks, possibly results in a resolution event. The direct resolution parameter is expressed as:

$$\delta_{resol.} = \sigma_s(n, He)\phi(E_n), \tag{9}$$

where, $\sigma_s(n, He)$ is the neutron scattering cross-section for helium, and ϕ_n is the neutron flux with energy E_n. Considering the 14 MeV neutron-helium scattering cross-section of 10^{-28} m^2 [107] and an approximate neutron flux of 10^{17} $m^{-2}s^{-1}$ on the divertor [108], the direct resolution parameter is of the order 10^{-11} s^{-1}.

2.8. Irradiation induced defect production rate

The production of point defects by neutron irradiation occurs by the displacement of a primary knock-on atom (PKA) followed by cascade formation and sub-cascade branching events, thereby representing a phenomenon scaling 18 orders of magnitude in time [109]. Thus, to accurately describe the evolution of defects at longer time scales (longer than seconds), the input defect production rate in the cluster dynamics model is essential. Following the work of Mannheim et al. [18], the defect production term in the model is expressed in terms of a power law relating the cluster frequency and cluster size as demonstrated by Sand et al. [110] and Yi et al. [111], and accounts for the production of point defects in isolated as well as clustered form:

$$G_{\theta_n} = \frac{A_\theta}{n^{S_\theta}}, \tag{10}$$

where, G_{θ_n} is the occurrence frequency of a defect cluster of size n, A_θ denotes the pre-factor associated with the total defect production rate, S_θ represents the scaling exponent and θ denotes the defect type i.e. *V* based or *I* based. The scaling exponents of the power-law from the work of Sand et al. [110] and Yi et al. [111] are only applicable at low temperatures ($\leq$30 K), whereas according to the MD simulations of Setyawan et al. [112], it is well established that the defect cluster production phenomenon is temperature sensitive. Here, a temperature dependency of the defect production rate is incorporated in the current work.

The temperature dependent total defect production rate G_0 is determined by weighing the primary knock-on atom energy spectrum by the number of surviving Frenkel pairs per PKA energy, based on the work of Mannheim et al. [18]. The estimated temperature dependent total defect production rate is summarized in Table 1 and a moderate temperature dependency is observed. The temperature dependent S_V and S_I exponent of the power law for the vacancy and interstitial cluster production are estimated based on the average unclustered vacancy (V), and SIA (I) fraction. The prefactors A_I and A_V of the power law are further evaluated in terms of the total defect production rate as:

$$A_\theta = \frac{G_0}{\sum_{n=1}^{N_{max}} n^{1-S_\theta}}, \tag{11}$$

where θ denotes the defect type, i.e. V based or I based clusters. The parameters G_0, S_V and S_I for temperatures other than mentioned in Table 1, are determined by linear interpolation.

Furthermore, to account for the net decrease in the defect production rate over time, i.e. the formation of cascades in areas with high defect population, the defect production rate G_0 is considered to decrease linearly with the defect fraction (f_θ) in the material. Additionally, the re-occurrence of cascades and the associated thermal spikes in areas with high defect density will also assist in recombinations of existing defects. Thus, a spike efficiency (ε_{th}) factor quantifying the thermally assisted recombinations is used for correction of the defect production rate. The spike efficiency (ε_{th}) depends on the volume of the thermal spike region (function of PKA energy), which is based on the work of Kaoumi [113] along with the fraction of defects present within the thermal spike volume. As a first order approximation, the spike efficiency is assumed to be of the order 10^{-3}. Accounting for the corrections, the defect production rate is expressed as:

$$G_{V_m/I_n} = \frac{A_{V_m/I_n}}{n^{S_{V_m/I_n}}}(1 - f_\theta / \varepsilon_{th}). \tag{12}$$

2.9. Helium implantation rate

For ITER-like conditions, the incoming energy of the helium ions is approximated to be within the range of 100–250 eV [32,114–116]. Since the energy of helium ions is well below the displacement threshold for tungsten (W), defect production by helium ions is not likely to occur. To address the depth dependent distribution of helium, the ion range distribution can be obtained via binary collision approximation codes (such as SRIM/TRIM) or MD simulations. The dependence of the implantation depth distribution on the substrate crystal orientation, substrate temperature and ion energy in tungsten has been well reported in literature via MD simulations of Borovikov et al. [24], and Hammond and Wirth [117]. However, for ion energies greater than 80 eV, the difference between the SRIM and MD based implantation depth profiles is minimal. Therefore, the SRIM based depth profiles are used as standard input in the present model. Fig. 3 shows the depth distribution of He ions implanted as simulated using the SRIM/TRIM code in quick damage calculation mode for an ion energy of 100 eV. For a specific depth, the time dependence of the helium production rate is expressed as:

Table 1
Defect production rate G_0, and scaling exponents (S_V,S_I) determined for temperatures used in MD simulations [112]; based on the work of Mannheim et al. [18].

T [K]	G_0 [dpa s^{-1}]	S_V	S_I
300	4.2×10^{-8}	1.63	2.20
1025	3.3×10^{-8}	1.86	2.50
2050	3.1×10^{-8}	2.42	2.17

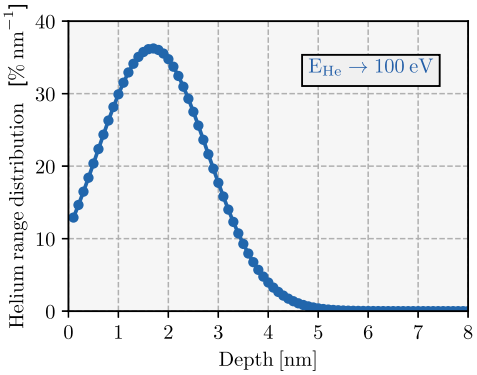

Fig. 3. Helium-ion range distribution for an ion implantation energy of 100 eV; simulated using the SRIM/TRIM code in quick damage calculation mode [118].

$$G_{He} = A \times \phi_{He}, \tag{13}$$

where G_{He} is the volumetric helium production rate, A is the production probability and ϕ_{He} is the ion flux. For longer irradiation time scales (≈years), the nuclear transmutation based helium production will occur uniformly along the entire monoblock but at a relatively slow rate. Hence, the transmutation assisted helium production source is ignored.

2.10. Volumetric stored energy

The defect size distribution at each node (point) along the monoblock depth is used to obtain a measure of the volumetric stored energy. The volumetric stored energy at a specific depth is calculated using the concentration of the defects (clusters and dislocations), as[2]:

$$E_{VS} = \sum_{m=1}^{M_V} C_{V_m} E^f_{V_m} + \sum_{n=1}^{N_I} C_{I_n} E^f_{I_n} + \sum_{n=1}^{N_{He}} C_{He_n} E^f_{He_n} + \sum_{n=1}^{N_{He}} \times \sum_{m=1}^{M_V} C_{He_nV_m} E^f_{He_nV_m} + \frac{1}{2}\mu b^2 \rho_n, \tag{14}$$

in which E_{VS} is the volumetric stored energy at a specific depth and time instance, C_θ is the associated concentration for a defect type θ and E^f_θ is the formation energy of defect type θ, with θ being V_m/I_n/He_n/He_nV_m.

2.11. Numerical implementation

The defect evolution in the monoblock bulk is described by a coupled set of ordinary and partial differential equations (ODEs-PDEs), see eq. (1). To solve this coupled system of equations, the PDEs representing the mobile defects are transformed into a system of ODEs by using the method of lines (MOL) approach [119], wherein the spatial derivative is expressed in terms of an algebraic approximation. Considering the dominant one dimensional temperature gradient in the monoblock [120], the spatial domain is discretized along a single dimension, corresponding to the monoblock depth (between points S and B in Fig. 4a) using a centered

[2] For the calculations of volumetric stored energy, the contributions of the configurational entropy are small and thus neglected.

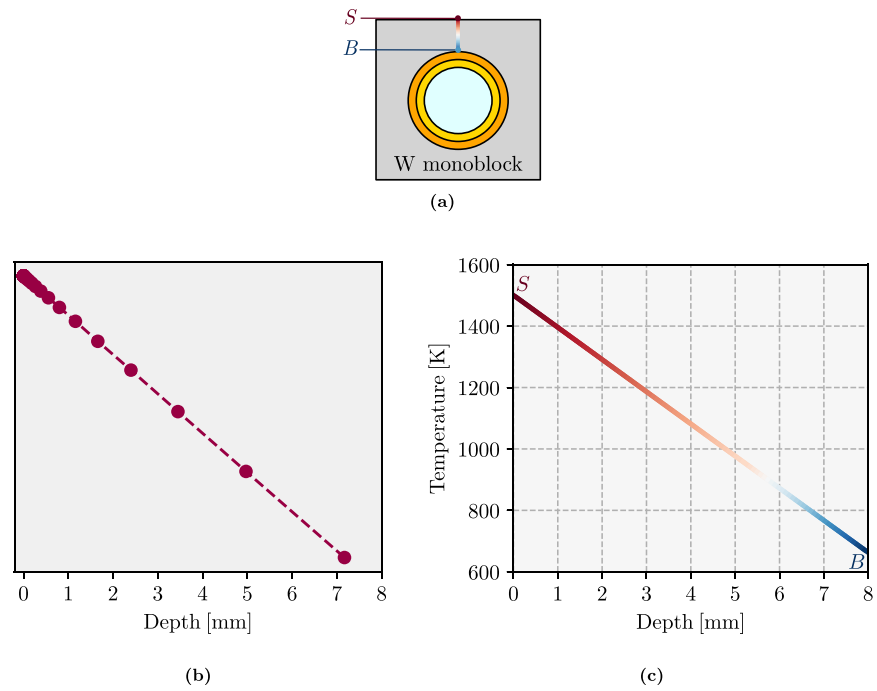

Fig. 4. **(a)** Spatial domain along the monoblock depth (S–B) simulated in the present model. **(b)** Discretization with a non-uniform grid. **(c)** Temperature gradient along the spatial domain for a steady state heat load of 10 MWm^{-2}, based on the thermo-mechanical analysis of ITER monoblocks [120]. (For interpretation of the references to colour in this figure legend, the reader is referred to the web version of this article.)

finite difference approximation on a non-uniform grid with N_x nodes, with the grid spacing increasing between the nodes at larger depths in the spatial domain. The spatial derivative term for a given mobile defect along the non-uniform grid is approximated as:

$$\frac{\partial}{\partial x}\left(D_\theta \frac{\partial C_\theta}{\partial x}\right) = \frac{2}{x^{i+1} - x^{i-1}}\left[D_\theta^{i+\frac{1}{2}} \frac{C_\theta^{i+1} - C_\theta^{i}}{x^{i+1} - x^{i}} - D_\theta^{i-\frac{1}{2}} \frac{C_\theta^{i} - C_\theta^{i-1}}{x^{i} - x^{i-1}}\right], \tag{15}$$

where, C_θ is the concentration of the mobile defect, D_θ is the spatially varying diffusion coefficient, x^i is the grid location and i is the node (point) number. The term $D^{i+\frac{1}{2}}$ represents the average of the diffusion coefficient between the grid locations i+1 and i. Fig. 4a and Fig. 4b schematically show the spatial domain along the monoblock depth and the distribution of the nodal points along the non-uniform grid. The diffusion coefficient for a given mobile defect is evaluated considering the temperature gradient resulting from a steady state heat load of 10 MWm^{-2} (Fig. 4c), relevant to ITER. The evolution of defects in the monoblock will also assist in the deterioration of the thermal conductivity in the monoblock, thereby affecting the overall temperature profile in the monoblock. However, in the present case, the evolution of the temperature profile in the monoblock as a function of the defect concentration is not accounted for.

The equilibrium concentrations of the defects are considered as the initial condition. Furthermore, two different types of boundary conditions with respect to the monoblock geometry are used. At the surface of the monoblock (i.e. point S in Fig. 4a), the concentration of defects is considered to be zero (Dirichlet - type), implying that the surface acts as a perfect sink. A Neumann-type zero flux boundary condition is used in the bulk (point B in Fig. 4a) because of the W–Cu interface, which can act as a diffusion barrier. The assumption of zero flux of helium atoms across the interface is motivated by the increase in the diffusion resistance in copper (Cu), as demonstrated by DFT calculations of De-shun et al. [121].

In the present model, the maximum number of each defect species is considered to be constant and the total number of ODEs in the system is given by $(M_V + N_I + N_{He} + N_{He} \times M_V + 3) \times N_x$, which is of the order 10^4. The time integration of the ODEs is performed using the multi-step variable-order time stepping solver CVODE based on the Backward Differentiation Formula (BDF) for stiff equations, from the SUNDIALS suite [122]. Furthermore, the equations are evaluated using a relative tolerance of 10^{-3}. Appendix A.6 provides the details of the simulation parameters used in the present model.

3. Results

In this section, the results from the spatially dependent cluster dynamics model with variations through the monoblock depth and at long irradiation time scales are presented. In Section 3.1, the evolution of defect concentration taking into account the mobility of small He_n clusters is shown. Thereafter, in Section 3.2, the mobility based influence of the small He_n clusters on the overall defect concentration is presented. Additionally, in Section 3.3, the evolution of the network dislocation density and the overall stored energy in the monoblock is illustrated and finally, in Section 3.4, the influence of helium detrapping and resolution from the microstructural sinks and defect clusters on the overall helium diffusion length scales is reported, and compared with the case without the detrapping and resolution mechanism.

3.1. Defect evolution in the monoblock at longer irradiation times

Fig. 5 shows the evolution of point defect clusters and the helium based clusters in the monoblock bulk following 1000 hours of irradiation, taking into account the mobility of vacancies (V), self-interstitial atoms (I), di-interstitials (I_2) and the small helium clusters (He_n). The defect concentration of V_m, I_n and He_n based

clusters is expressed as the cumulative sum over the total number of atoms inside the defect cluster ($\sum_{n=1}^{max} nC_n$). As observed in Fig. 5a, the diffusion of helium atoms extends into the monoblock bulk, with a diffusion length scale corresponding to approximately 0.5 mm after 1000 hours of irradiation. Furthermore, immobilization of V_m based clusters by He_n clusters and the associated clustering reactions results in the formation of mixed He_nV_m clusters, with relatively high concentrations in the surface and sub-surface layers of the monoblock (see Fig. 5b). The concentration of mixed He_nV_m clusters reduces further along the monoblock depth due to the scarcity of *He* atoms.

Simultaneously, the *V* concentration in the surface and sub-surface layers of the monoblock is lowered by the combination of *V* trapping by He_n, He_nV_m clusters and the microstructural sinks. In the monoblock bulk, the total V_m concentration increases due to negligible trapping at He_n and mixed He_nV_m clusters. Additionally, the nearly constant concentration of V_m in the depth region ($\approx$ 5–8 mm) can be attributed to the lower temperatures in the bulk (700–900 K), thereby lowering the mobility of vacancies (*V*), and hence lowering the *V* losses by reduced frequency of *V*-V_m based clustering events and decreased flow to the microstructural sinks. Also, the highly mobile SIAs at lower temperatures facilitate the V_m-I_n ($n \leq 2$) recombination events, ultimately resulting in a concentration plateau for V_m in the bulk.

A large proportion of the injected *He* atoms are trapped as He_nV_m clusters. Besides the mixed He_nV_m clusters, the total *He* concentration in He_n based clusters and at microstructural sinks (He_{sinks}) is nearly identical in the near surface region of the monoblock and diverges in the bulk, with moderately higher *He* concentration at the sinks than in the He_n based clusters. Fig. 6 shows the temporal evolution of *He* concentration at the sinks through the monoblock depth. The increase in *He* concentration at the microstructural sinks can be rationalized based on the lowering of trapping events between the mobile *He* defects and the point defects, along with an increase in trapping of mobile *He* based defects at the microstructural sinks for longer irradiation times (> 200 hours). Furthermore, with respect to the monoblock length scale (and the associated temperature gradient), and irrespective of the spatial location, the concentration of the He_nV_m clusters is always higher compared to that of the clusters and *He* at sinks, thereby demonstrating the strong affinity of *He* atoms and vacancies (*V*) towards clustering.

Fig. 7 schematically shows the distribution of the mixed He_nV_m clusters at different locations in the monoblock as a concentration map after 1000 hours of irradiation. Only the concentration near the surface and in the sub-surface layers of the monoblock are shown, given the pronounced accumulation of *He* atoms in these layers. At smaller length scales of a few tens of nanometers (Fig. 7a), He_nV_m clusters with a relatively high number of *He* atoms (compared to the number of vacancies *V*) are formed, i.e. clusters with an *n/m* ratio greater than or equal to 1. Furthermore at monoblock depths ranging from a few hundreds of nm to μm (Fig. 7b–d), pre-dominantly smaller He_nV_m based clusters with a nearly equal number of *He* atoms and *V* are formed. The formation of small He_nV_m clusters at larger length scales (here, the sub-surface) is due to the limited amount of *He* atoms in these layers, thereby preventing the *He* assisted growth pathway of the He_nV_m clusters. The temporal evolution of He_nV_m clusters in the monoblock surface region is schematically shown in Fig. 8.

At irradiation time scales of a few seconds (Fig. 8a), the nucleation of small He_nV clusters occurs by pronounced trapping of vacancies (*V*) by the *He* atoms, and these clusters further grow predominantly by trapping of mobile clusters in addition to the mobile *V* (Fig. 8b). As the irradiation progresses, the trapping events between the mobile clusters, *V* and the existing He_nV_m clusters occur frequently, ultimately leading to clusters with an *n/m* ratio greater than or equal to 1. The evolution trend of the He_nV_m clusters at irradiation time scales of hours, as shown in Fig. 8c and d, does not change substantially, and this can be attributed to the constrained cluster space of the He_nV_m clusters. However, the concentration of *He*-rich He_nV_m clusters varies marginally with time by inter-cluster emission-trapping based exchange of *He* atoms.

3.2. Mobility based influence of helium clusters on the defect evolution

Fig. 9 depicts the evolution of defects after 1000 hours of irradiation, for the case where the mobility of *V*, *I*, I_2 and *He* atoms is accounted for, and the small He_n clusters are considered as immobile species. The concentration of V_m, I_n and He_n clusters in Fig. 9 reveals the sum over the number of atoms inside the cluster, as described previously. As seen in Fig. 9a, the helium diffusion length scales and associated concentrations of the helium based defects in the monoblock are relatively higher, when only the mobility of the *He* atoms is incorporated for, in contrast to the previous case (Fig. 5a). Comparing Fig. 5 (with the mobility of He_n clusters) with Fig. 9 (without the mobility of He_n clusters), it can be

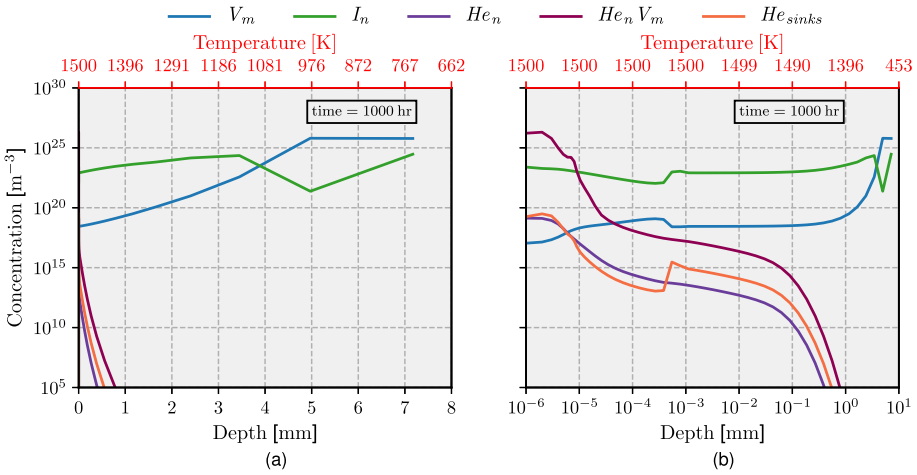

Fig. 5. Evolution of defects following irradiation time of 1000 hours, simulated with the mobility of vacancies (*V*), self-interstitial atoms (*I*), di-interstitials (I_2) and helium based clusters (He_n) **(a)** Semi-log plot **(b)** Log-log plot. The concentration of V_m, I_n and He_n clusters is expressed as the total concentration by summing over the number of atoms inside the defect cluster. (For interpretation of the references to colour in this figure legend, the reader is referred to the web version of this article.)

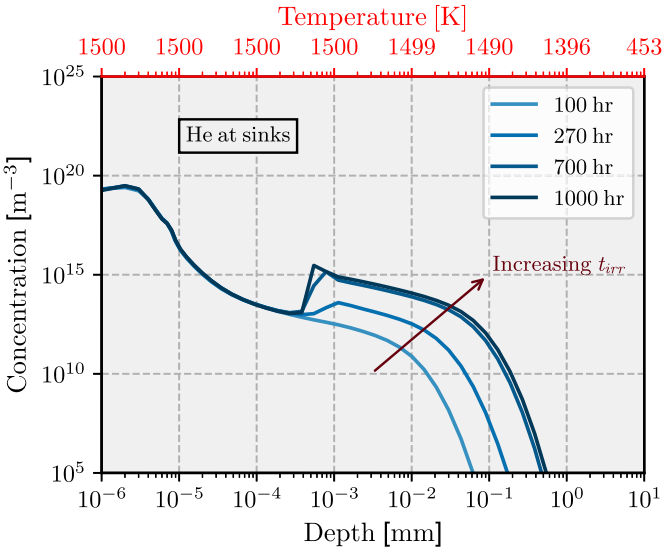

Fig. 6. Evolution of *He* concentration at the microstructural sinks along the monoblock at different irradiation time instances. The increase in *He* concentration at longer irradiation times is due to increase in trapping events of mobile *He* based clusters at the microstructural sinks as compared to the point defects. (For interpretation of the references to colour in this figure legend, the reader is referred to the web version of this article.)

observed that the mobility of the He_n clusters restricts the penetration of *He* atoms into the bulk for similar irradiation time scales. In Fig. 5 relatively high concentrations of helium based defects (He_n, He_nV_m, He_{sinks}) are observed near the surface (up to 100 nm), followed by a gradual reduction in concentrations deeper in the bulk (more clearly visible in Fig. 5b). Moreover, this trend is significantly different when the He_n clusters are not mobile (Fig. 9), where nearly a constant concentration of helium based defects is observed along the surface and sub-surface layers of the monoblock, thereby highlighting the prominent influence of the mobile He_n clusters on the overall helium retention in the monoblock. Additionally, the lower helium retention in the monoblock with mobile He_n clusters can be rationalized based on the formation of small He_n based clusters near the monoblock surface by pronounced clustering of *He* atoms, which remain mobile and therefore also, contribute to the desorption based loss of *He* atoms at the surface. The prominent reduction in the overall helium retention under the influence of mobile *He* based defects and for a similar helium ion flux as considered here, has also been observed by Perez et al. [77]. Although, in this study the *He* atoms and small *HeV* based cluster were assumed to be mobile, the underlying physics behind the overall lower retention levels is not significantly affected.

In Fig. 9 (excluding mobile He_n clusters), a relatively larger proportion of the injected *He* atoms are retained in the monoblock as compared to Fig. 5 (with mobile He_n clusters). Accordingly, the trapping events between the mobile *V*-He_n and the associated clustering events occur frequently, thereby increasing the recur-

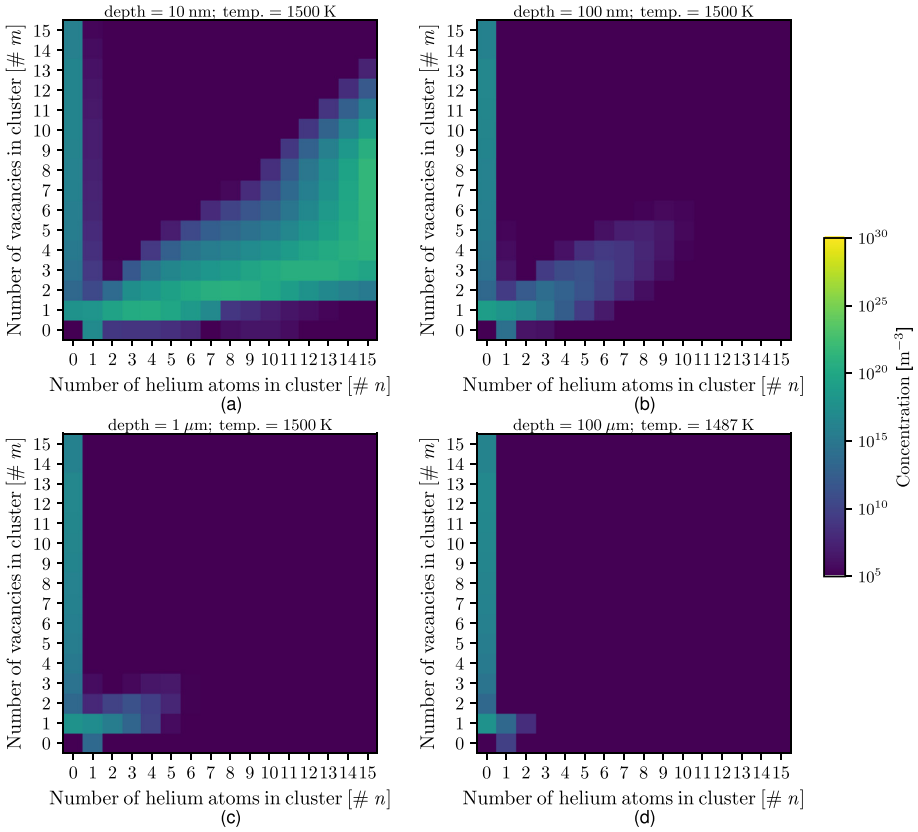

Fig. 7. Concentration maps showing the distribution of He_nV_m clusters at different depths in the monoblock after irradiation of 1000 hours; considering small He_n clusters as mobile species **(a)** 10 nm **(b)** 100 nm **(c)** 1 μm **(d)** 100 μm. (For interpretation of the references to colour in this figure legend, the reader is referred to the Web version of this article.)

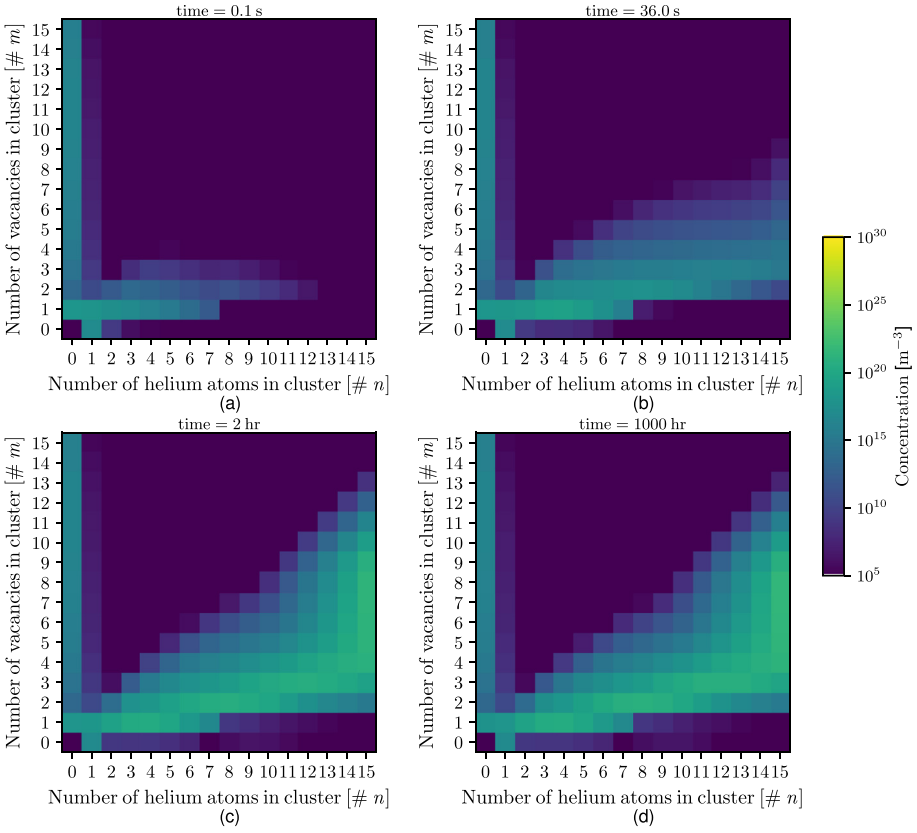

Fig. 8. Temporal evolution of He_nV_m clusters considering He_n clusters as mobile species at depth of 10 nm in the monoblock, after irradiation times of 1000 hours **(a)** 0.1 s **(b)** 36 s **(c)** 2 hr **(d)** 1000 hr. (For interpretation of the references to colour in this figure legend, the reader is referred to the web version of this article.)

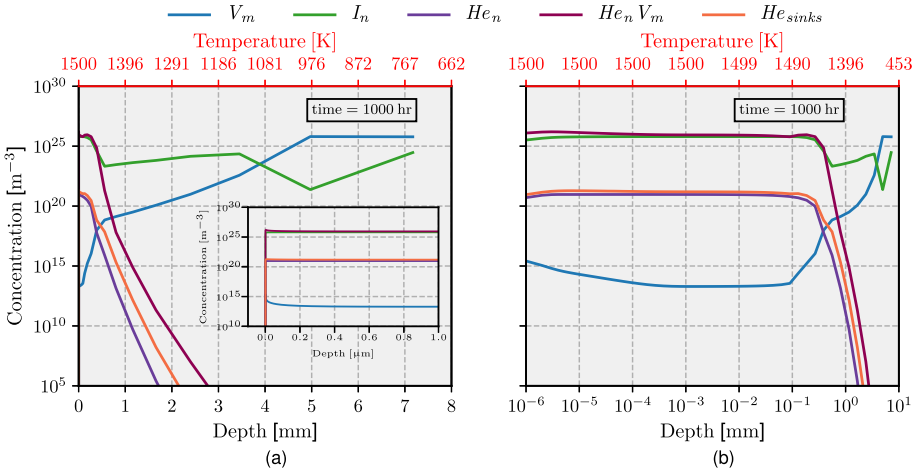

Fig. 9. Evolution of defect concentrations along the monoblock depth after 1000 hours of irradiation with mobile vacancies (V), self-interstitials (I), di-interstitials (I_2) and helium atoms (He); **(a)** Semi-log plot **(b)** Log-log plot. The concentration of V_m, I_n and He_n clusters is expressed as the total concentration by summing over the number of atoms inside the cluster. The inset in **(a)** displays the zoomed defect concentration profile near the monoblock surface, with a null concentration (Dirichlet-type) boundary condition enforced at the surface. (For interpretation of the references to colour in this figure legend, the reader is referred to the web version of this article.)

rence of the V immobilization events. The increase in the V immobilization events further imply an overall decrease in the total V concentration (Fig. 5b) in the monoblock and conversely an increase in the total I concentration (Fig. 5b) due to the lower probability of V-I recombination events.

In the bulk of the monoblock (> 1 mm), the depth dependent evolution, more specifically the temperature dependent concentration profile of the V and I defects is identical in both cases, i.e. either with immobile small He_n clusters (Fig. 9) or with mobile He_n clusters (Fig. 5). Likewise, the distribution of the injected He atoms is identical in both cases, with a higher proportion of He atoms present as He_nV_m clusters.

3.3. Evolution of dislocation density and volumetric stored energy in the monoblock

The network dislocations act as sinks for the irradiation induced mobile point defects (V, I, I_2), and their evolution in the monoblock is therefore coupled with the evolution of the irradiation point defects. Fig. 10 displays the evolution of the network dislocation density in the monoblock after 1000 hours of irradiation with mobile small He_n clusters. Fig. 10a and fig. 10b, show that at the monoblock surface, the density of the network dislocations is nearly equal to the initial dislocation density, with small reductions in density. For depths greater than 100 nm, the density of the dislocations increases, followed by a drop to the initial dislocation density in the bulk of the monoblock (5 mm). This dislocation density evolution can be related to the difference in climb velocity of the dislocations along the monoblock depth, which is directly dependent on the concentration of the mobile point defects (which is a function of temperature). At the monoblock surface, the evolution of the dislocation density is minimal as the BH source based generation rate and the dipole annihilation rate roughly balance each other. The increase in the dislocation density at larger depths (>100 nm) is due to the higher BH source based dislocation generation rate, specifically governed by the balance between the mobile point defects, i.e. the concentration of V and I based defects (as shown in the inset in Fig. 10b). The consequences of the higher mobile point defect concentration (pre-dominantly vacancies V) for the evolution of the network dislocation density are most prominent at depths of $\approx$ 500 nm–5 mm, resulting in relatively higher network dislocation densities along the monoblock depth. In general, the highest dislocation density in the monoblock is observed in the temperature range 1100 K–1150 K with a magnitude reaching as high as 10^{16} m^{-2}.

From the evolution of the dislocations and the defect clusters, the volumetric stored energy in the monoblock can be quantified. Fig. 11 depicts this depth profile of the volumetric stored energy for irradiation time of 1000 hours. The stored energy profile shows a peak at the monoblock surface with substantially high values of the order 10^8 Jm^{-3}, with a significant drop in the sub-surface layer, followed by a gradual increase in the monoblock bulk. To obtain a better understanding of the evolution of the stored energy, the contributions from the individual defect classes are assessed. Fig. 12 shows, that at the monoblock surface, the largest contribution to the stored energy profile stems from the He_nV_m clusters. At larger depths, the major contributers to the stored energy profile are the I_n clusters, dislocations, and V_m clusters (in this order for increasing depths) with lower magnitudes as compared to He_nV_m clusters.

3.4. Influence of helium detrapping and resolution on the diffusion length scales

Fig. 13 shows the influence of the helium (He) detrapping and resolution mechanisms on the evolution of He based defects along the depth of the monoblock after 400 hours of irradiation, with He_n clusters as mobile species. In Fig. 13a, the detrapping and resolution of He atoms from the microstuctural sinks and defect clusters is not incorporated. In that case, the diffusion of helium in the monoblock bulk is limited, thereby resulting in the formation of He_n and He_nV_m clusters up to a depth of a few μm. Moreover, the limitation on the diffusion of helium in the bulk monoblock arises from the high mobility of the He atoms in the monoblock surface (high temperatures), thereby leading to pronounced trapping events at the microstructural sinks, as visible in Fig. 13a. The increased trapping of He atoms at the microstructural sinks ultimately lowers the amount of He atoms available for free diffusion.

On the contrary, when the detrapping and resolution of He atoms from the microstructural sinks and defect clusters is taken into consideration, a substantial increase in the He diffusion length scale emerges, i.e. nearly up to 0.5 mm (Fig. 13b) as compared to tens of μm (Fig. 13a). In addition, substantially higher concentrations of He atoms are present in the form of He_n and He_nV_m clusters through the monoblock depth. The increase in the diffusion length scale and the overall He concentration in the monoblock is due to the abundance of mobile He atoms in the grain interior (matrix), which further undergo self-clustering, V immobilization as well as diffusion based events in the monoblock bulk. In fact, the innate consequence of the He detrapping and resolution mechanism is a reduction of the overall He concentration at the microstructural sinks, see Fig. 13b. Furthermore, for higher irradiation fluences, without detrapping and resolution, as observed in the inset of Fig. 13a, the concentration of the He atoms at the microstructural sinks (at a depth of 10 nm) keeps increasing. On the other hand, considering the detrapping and resolution case, the concentration of He atoms at the microstructural sinks saturates, thereby resembling the expected physics for higher irradiation fluences. A

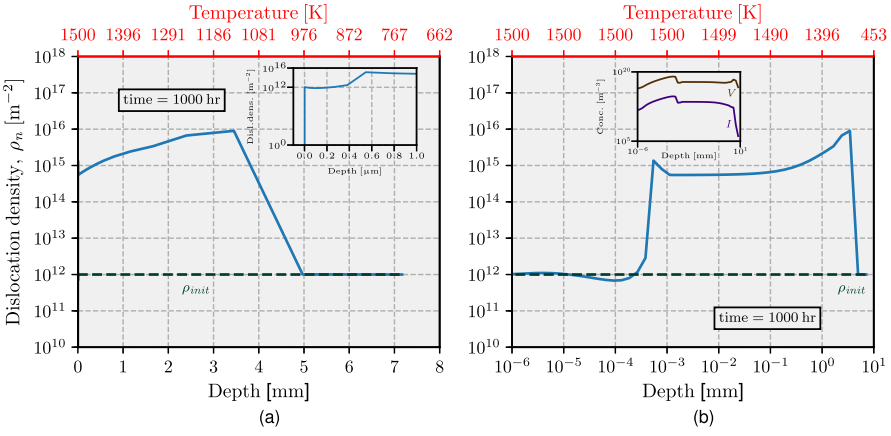

Fig. 10. Network dislocation density evolution in the monoblock simulated with mobile small He_n clusters, following 1000 hours of irradiation **(a)** Semi-log plot **(b)** Log-log plot; The line labeled ρ_{init} represents the initial dislocation density in the monoblock. The inset in **(a)** shows the evolution of dislocation density near the monoblock surface, with a zero concentration boundary condition enforced at the monoblock surface. The inset in **(b)** represents the total concentration of the V and I defects along the monoblock. (For interpretation of the references to colour in this figure legend, the reader is referred to the web version of this article.)

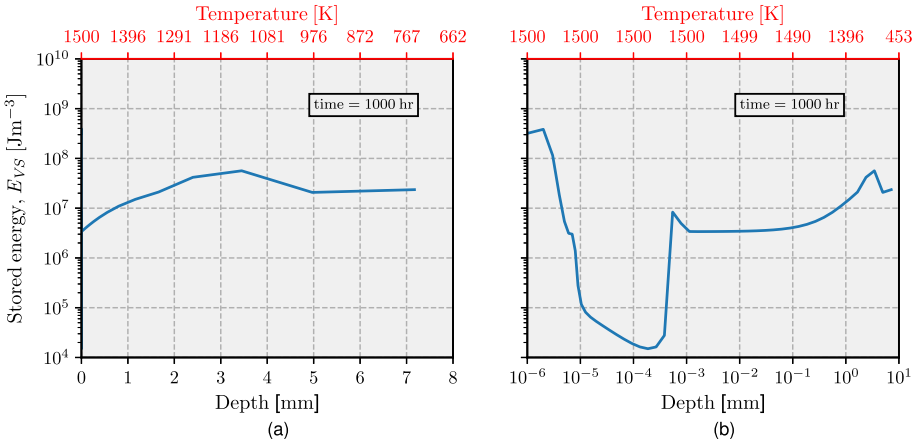

Fig. 11. Spatially varying volumetric stored energy in the monoblock following 1000 hours of irradiation with mobile small He_n clusters **(a)** Semi-log plot **(b)** Log-log plot.

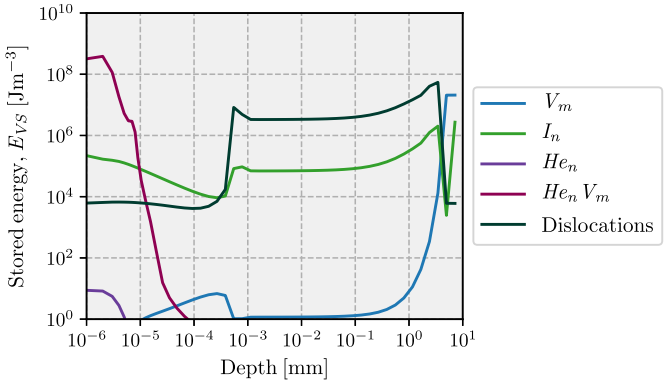

Fig. 12. Spatial profiles of the individual defect contribution to the volumetric stored energy shown in Fig. 11 after 1000 hours of irradiation depicted in a log-log plot. (For interpretation of the references to colour in this figure legend, the reader is referred to the web version of this article.)

similar conclusion with respect to the saturation of *He* accumulation at the grain boundaries and the detrapping of *He* atoms from the grain-boundaries at a higher fluence has also been drawn by Zhao et al. [58]. To gain further insight on sink dependent retention of *He* atoms (for the case including the detrapping and resolution of *He* atoms), Fig. 14 provides a comparison of the *He* atoms retained per grain boundary surface area and the dislocation line. Additionally, considering the retained *He* atomic fraction at the sinks, a relatively higher concentration of *He* atoms trapped at dislocations can be observed as compared to grain boundaries (Fig. 14). Moreover, irrespective of the sink type, the retained fraction of *He* atoms after 400 hours irradiation is smaller than 1 (Also, for irradition time of 1000 hours, the *He* atomic fraction at the sinks is smaller than 1; not shown here). However, heterogeneous nucleation of *He* bubbles at the sinks may occur for reactor-like timescales ($\approx$ years). Note that with respect to the individual contributions of the *He* detrapping and resolution mechanism on the diffusion length scales, the contribution from the detrapping based mechanism is dominant compared to the resolution based mechanism (not shown here), due to the relatively lower resolution frequency of the *He* atoms from the microstructural sinks and defect clusters.

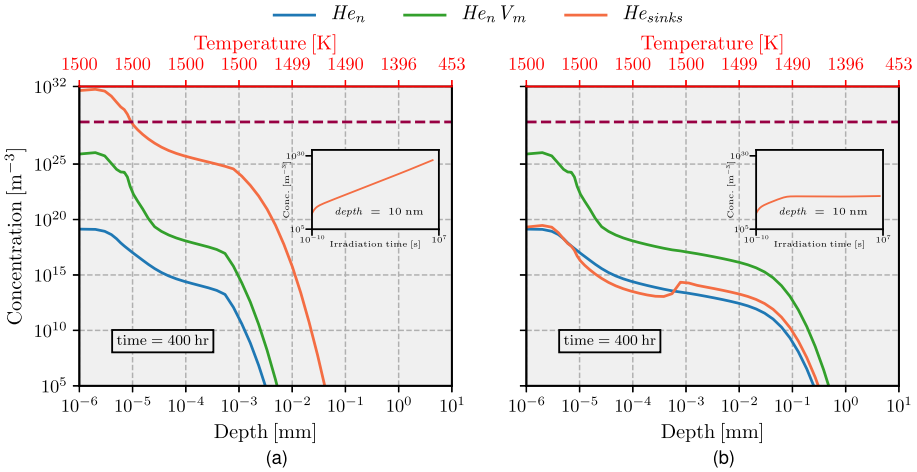

Fig. 13. Evolution of *He* based defects (He_n, He_nV_m, He_{sinks}) along the monoblock depth after 400 hours irradiation time for two different cases: **(a)** without *He* detrapping and resolution from the microstructural sinks and defect clusters **(b)** with *He* detrapping and resolution from the microstructural sinks and defect clusters; The insets in **(a)** and **(b)** show the temporal evolution of the *He* concentration at the microstuctural sinks at a depth of 10 nm. The dashed purple line in **(a)** and **(b)** represents the W atomic density and defines the limit in terms of the maximum defect concentration. For the case, i.e. without *He* detrapping and resolution **(a)**, the assumption of infinite sinks ultimately results in a physically unrealistic *He* concentration at sinks. (For interpretation of the references to colour in this figure legend, the reader is referred to the web version of this article.)

3.5. Influence of cluster size on defect evolution

In the previous sections, the evolution of defects in the monoblock, simulated using a maximum cluster size of 15 and a few hundred hours of irradiation were presented. In this section, the influence of the maximum cluster size on the defect evolution trend is assessed.

Fig. 15 shows the spatially dependent concentration of different defects in the monoblock as a function of varying maximum cluster size (15, 25 and 35) after 25 hours of irradiation. As seen in Fig. 15, for similar irradiation time scale, the concentration trend of the He based defects, i.e. He_n clusters, He_nV_m clusters as well as the *He* atoms trapped at sinks are nearly similar, indicating a negligible influence of the cluster size on the defect evolution trend. Also, irrespective of the simulated maximum cluster size case, the diffusion length scales of the *He* atoms are identical, restricted up to a few hundred micrometer. The concentration profiles of V_m and I_n, specifically in the surface and sub-surface region of the monoblock show identical behaviour independent of the maximum cluster size. However, in the monoblock bulk, i.e. approximately > 0.5 mm, the depth dependent evolution trend reveals a weak dependency on the maximum cluster size. As the maximum cluster size increases, the overall concentration of the V_m based clusters also increases with a relatively smoother trend-line, and correspondingly, the overall concentration of the I_n based clusters diminishes.

Furthermore, to investigate the influence of the maximum cluster size on the nature of He_nV_m clusters, the distribution of He_nV_m clusters near the surface of monoblock (depth: 10 nm) after 25 hours of irradiation for different size cases are shown in Fig. 16. As stated previously (Section 3.1), the He_nV_m clusters in Fig. 16 predominantly tend to be of a type with a n/m ratio greater than 1, i.e. highly pressurized bubbles, irrespective of the maximum cluster size. Moreover, from the evolution of the He_nV_m cluster with an increase in the maximum cluster size, it can be concluded that the assumption of smaller maximum cluster size for higher doses artificially restricts the concentration of the clusters near the border of the cluster space, thereby providing inaccurate information on the nature of He_nV_m clusters. It is important to point out that this restriction also holds true for the defect classes such as V_m and I_n clusters. Nevertheless, for the present case, since the assumption of smaller maximum cluster size has a negligible influence on the defect evolution trend in the monoblock (Fig. 15), a qualitative insight on the defect evolution trend in the monoblock can still be obtained.

4. Discussion

In this paper, the diffusion length scale of *He* atoms in the monoblock bulk at irradiation time scales of hours was investigated for the first time. The diffusion of *He* atoms in the bulk monoblock was found to occur up to the millimeter length scale, in conjunction to their trapping at the neutron induced lattice defects in the surface and sub-surface of the monoblock. The diffusion length scale of *He* atoms was observed to be dependent on the mobility of small He_n clusters, with lower diffusion length scales when the He_n clusters are mobile.

Similarly, the overall helium retention in the monoblock was also found to be dependent on the mobility of the small He_n clusters. The overall helium retention was lower when the He_n clusters were mobile. This lower helium retention in the monoblock was due to the increased losses of *He* atoms (in the form of He_n clusters) at the monoblock surface, and was in accordance with numerical studies investigating the influence of helium based cluster mobility on the overall helium retention for ion fluxes relevant for ITER conditions. Furthermore, the limited diffusion of *He* atoms in the bulk monoblock was caused by a combination of higher losses of *He* atoms at the surface and pronounced clustering of *He* atoms with the irradiation induced vacancies (V) in the near surface region of the monoblock. This implies that at high temperatures and with continuous irradiation, the trapping based mechanism of helium atoms at vacancies dominates over the diffusion of *He* atoms. A clear influence of the limited helium diffusion on the distribution of the He_nV_m clusters was also noticed, entailing the formation of small helium-vacancy (HeV) clusters in the bulk, conversely to the formation of helium rich He_nV_m clusters in the near surface region of the monoblock due to surplus of helium atoms.

For longer irradiation times, the detrapping of *He* atoms from the microstructural sinks was introduced in the present model and leads to a saturation of the *He* concentration at microstructural sinks. Moreover, the direct resolution of *He* atoms from the defect clusters and sinks by neutrons was taken into consideration. The influence of the detrapping and resolution based mechanism on the diffusion length scale of *He* in the monoblock bulk was investigated, and a significant increase in the diffusion length scales of helium atoms in the monoblock was identified. The influence of these mechanisms on the *He* diffusion length scales has not been reported previously and should be taken into account to capture the relevant processes for higher irradiation fluences. The extended *He* diffusion into the monoblock and the associated formation of the He_nV_m clusters (bubbles), especially at longer irradiation time scales can have detrimental consequences, such as a reduction in thermal

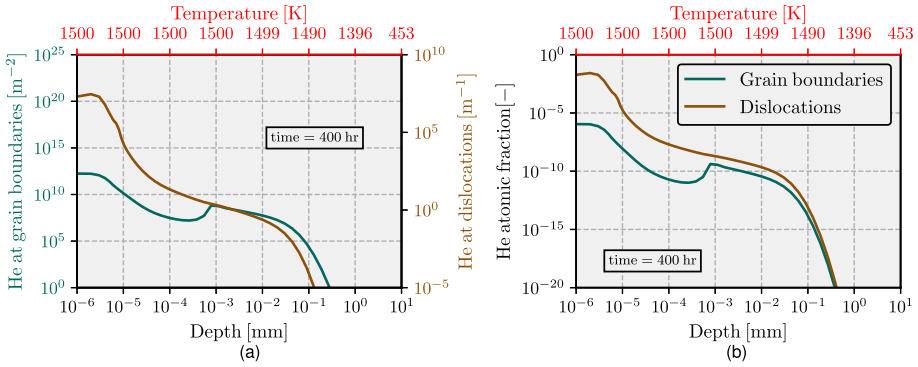

Fig. 14. Spatially dependent microstructural sink retention of *He* following irradiation time of 400 hours (from Fig. 13, orange coloured line), as a function of sink nature, i.e. grain boundaries and dislocations **(a)**, and compared in terms of atomic fraction (**b**). (For interpretation of the references to colour in this figure legend, the reader is referred to the web version of this article.)

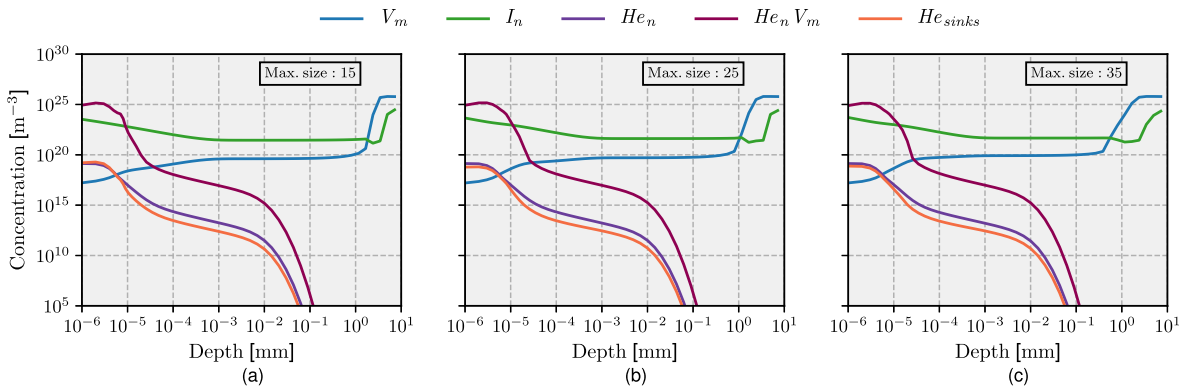

Fig. 15. The concentration profiles of different defects in the monoblock following 25 hours of irradiation as a function of the maximum cluster size **(a)** 15, **(b)** 25 and **(c)** 35. (For interpretation of the references to colour in this figure legend, the reader is referred to the web version of this article.)

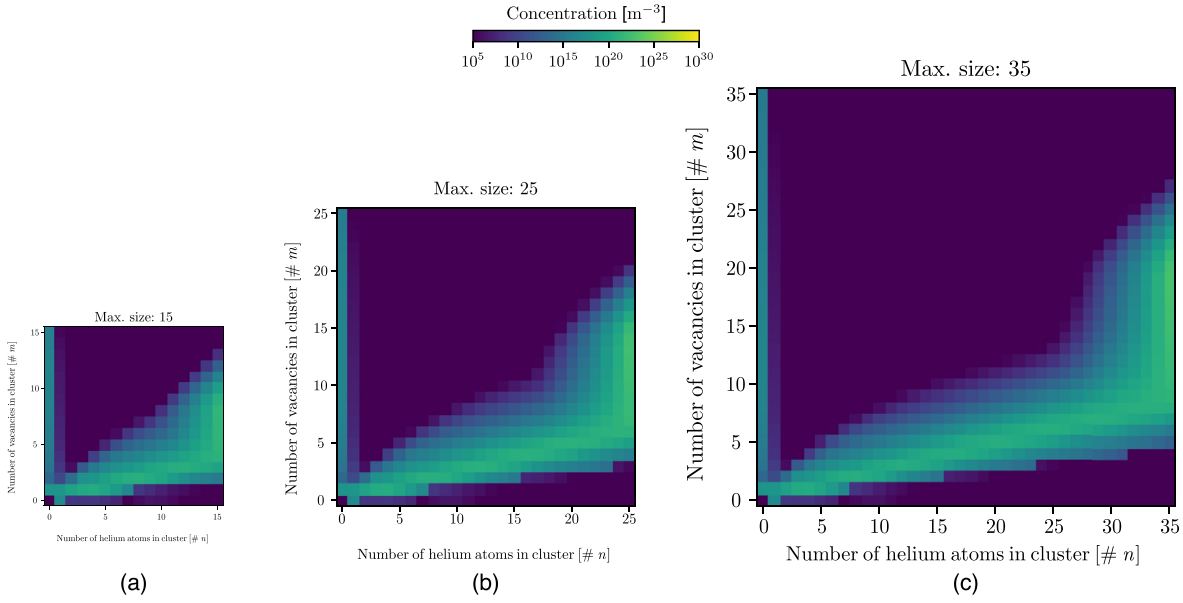

Fig. 16. The distribution of He_nV_m clusters at a depth of 10 nm in the monoblock following 25 hours of irradiation simulated using varying maximum cluster size **(a)** 15, **(b)** 25 and **(c)** 35. (For interpretation of the references to colour in this figure legend, the reader is referred to the web version of this article.)

conductivity, and strength and embrittlement of the monoblocks under operation. Additionally, transmutation assisted uniform generation of helium gas at irradiation time scales of years (which was not considered here) can aggravate this situation by providing an additional source of helium atoms in the monoblock.

The accumulation of irradiation defects in the microstructure leads to a non-equilibrium state of the microstructure, which at high temperatures may result in microstructure evolution by recrystallization and grain growth. The spatial profiles of the specific stored energy due to the accumulated concentration of defects in the monoblock after irradiation time scales of hours was observed to be in the range of 10^4-10^8 Jm^{-3}. Considering the results from the neutron-induced recrystallization model of Mannheim et al. [18], the material in the surface region of the monoblock is likely to evolve by recrystallization and grain growth. However, the precise evolution of the microstructure by recrystallization and grain growth in the presence of the helium bubbles is not clear. As mentioned earlier, the presence of helium bubbles can result in overall higher temperatures in the monoblock (through the decrease of thermal conductivity), which in combination with the high stored energies can result in recrystallization of the bulk monoblock. At the same time, the presence of helium bubbles as well as helium atoms at the grain boundaries can exert drag forces on the moving boundaries, thereby delaying the nucleation of the grains as well as their growth. In this regard, the influence of the high temperatures (present in the near surface regions of the monoblock) on the kinetics of recrystallization in the presence of helium based defects in the monoblock is also an important parameter to consider, and further studies are required to assess these microstructural interactions.

Full-scale experimental validation of the bulk effects described by the current model poses several challenges owing to the lack of a fast neutron source combined with a long exposure time (to attain high dpa) and handling of the neutron exposed samples. In this context, the use of high-energy protons as a surrogate for neutrons can be used for uniform defect generation at component length scales along with helium ion exposure to simulate fusion-relevant loading conditions. Despite these limitations, the model is already unique in capturing the interaction of neutron induced defects and helium atoms at length and time scales relevant for reactor operations, revealing the effect of the mobility of small He_n clusters on the overall helium retention in the monoblock. The influence of

helium detrapping from the microstructral sinks and resolution mechanism on the helium diffusion length scale is also featured in the current model. As highlighted earlier, the complete description of the microstructure evolution of tungsten monoblocks under combined neutron, plasma and heat loads requires not only a description of the damage accumulation in the microstructure, but also that of the microstructural recovery processes such as recrystallization and grain growth. Thus, for future work, the existing spatially dependent cluster dynamics model describing the evolution of neutron and helium based defects may be linked to a recrystallization model. This would allow to investigate the influence of the existing temperature gradient and the associated damage accumulation, especially the role helium bubbles on the microstructural recovery processes in the monoblock.

In the current model, for unravelling the physical mechanisms occurring under the combined neutron, plasma and heat load exposure, the defect clusters were limited to relatively small sizes, which is one of the limitations of the present model. Another limitation of the model is the omission of 1D migration of SIA clusters and the unfaulting of SIA loops into the network dislocations. Nonetheless, the present model provides a qualitative view on the defect evolution trend in a monoblock under synergistic neutron and ion irradiation. In terms of further improvement of the model, i.e. more accurate and quantitative description of microstructure evolution in terms of defects under irradiation, the defect cluster space (specifically for the case of helium bubbles) can be expanded by use of an approximation such as grouping or Fokker-Planck based scheme. The grouping scheme is based on grouping defects with similar properties into a super cluster, which is further represented by a pair of equations, i.e. the mean density of the super cluster and its first order moment [51]. Similarly, the Fokker-Planck scheme is based on representing the cluster distribution as a continuous function for a given size, and the evolution of the cluster distribution is tracked by an advection drift diffusion term. Although, both these schemes have their pros and cons, the grouping based implementation is relatively simpler as compared to Fokker-Planck, and also allows to tune the group width more easily without any issues related to the transition regime [123], thereby favoring the use of the grouping based scheme in our future work. Apart from the restricted cluster space, the extent of 1D diffusion of SIA clusters and the SIA loop unfaulting on defect evolution for reactor time and length scale has not been investigated thoroughly yet. Additionally, the dislocation half spacing dictating the climb velocity of the network dislocations was approximated to be independent of the evolving dislocation density, i.e. based on an upper bound dislocation density of 10^{16} m^{-2}. Although, this approximation is reasonable, accounting for the intrinsic relation between the dislocation half spacing and the evolving dislocation density is recommended and will be included in our future work. Also, in tungsten, studies on the grain boundaries and dislocations as fast diffusion pathways (i.e. grain boundary diffusion and pipe diffusion) for *He* atoms are not conclusive. Nevertheless, the fast diffusion of *He* atoms along these defects can be incorporated in the current model, thereby allowing to investigate the influence of faster diffusion pathways on the overall helium retention. Both the diffusion of hydrogen isotopes and their interaction with the neutron induced defects and *He* atoms, and the role of other impurities and transmutants as trapping sites for the defects were not accounted for in the current model. Thus, to extend the current defect evolution model, the interactions between the different plasma species, lattice defects and the impurities should be incorporated as well. Note, however that the incorporation of these interactions will increase the complexity of the model, the associated computational cost and the associated challenging demands for experimental studies to enable parameter identification as well as validation.

5. Summary and conclusions

A multi-scale model describing the microstructural evolution of tungsten monoblocks under combined neutron and helium loads in terms of defect concentrations, at component length scale and time scales relevant for reactor operation has been developed. The model is based on a cluster dynamics framework and accounts for the diffusion of mobile defects along the monoblock depth. In particular, special emphasis was placed on the diffusion of helium atoms (*He*) and the associated nucleation of helium-vacancy clusters (He_nV_m) by trapping at the lattice defects. The role of temperature on the defect evolution was addressed by considering a temperature gradient along the monoblock depth, corresponding to a steady state heat load of 10 MWm^{-2}. The main findings from the work are:

- The defect evolution simulated at longer irradiation and larger time scale reveals dominant formation of He_nV_m clusters (bubbles) in the sub-surface layers of the monoblock, due to significant trapping of *He* atoms at V_m defects, with relatively lower concentration in the monoblock bulk. The formation of V_m based clusters was dominant in the bulk monoblock, due to limited helium diffusion and relatively lower temperatures.
- The diffusion length scale of *He* atoms and the corresponding formation of *He* bubbles in the monoblock was observed to be strongly dependent on the neutron assisted resolution, the temperature driven detrapping from sinks as well as the mobility of He_n clusters. The inclusion of neutron assisted resolution and a temperature drive detrapping mechanism resulted in an increase in the helium diffusion length scales. When accounting for the mobility of the He_n based cluster, the overall diffusion length scales of *He* atoms are lower. Considering the irradiation time scale of few hundred hours, i.e. reactor time scale, and the representative physical mechanisms, the diffusion of *He* atoms extends to depths up to millimetres in the monoblock, thereby, highlighting the importance of neutron assisted resolution and temperature drive sink detrapping on the overall defect evolution.
- Within the context of the mobility of He_n based clusters, the overall helium retention in the monoblock was found to be susceptible to the mobility of the He_n based clusters. For the case of mobile He_n clusters, a lower concentration of the *He* and He_nV_m based clusters was found along the monoblock depth due to increased desorption losses from the monoblock surface.
- The defect evolution following irradiation in the monoblock was used to obtain a measure of the elastic stored energy. For reactor irradiation time scales, the elastic stored energy from defects was higher near the surface and in the monoblock bulk, with He_nV_m clusters and network dislocations being the major contributors. The stored energy profiles in the monoblock obtained in this study are qualitative in nature. Further studies considering the influence of the loop unfaulting on the population of network dislocations need to be performed for a more quantitative stored energy analysis in the monoblock.
- For longer irradiation time scales (higher doses), the influence of the maximum cluster size on the overall defect evolution and the helium diffusion length scale in the monoblock was observed to be minor. However, a significant influence on the distribution of V_m, I_n, He_nV_m clusters was observed, with an artificial restriction along the cluster space border, for the case when the simulated maximum cluster size was relatively small. This can be very important when extending the present model to simulate the size distribution of helium bubbles, loops and

their influence on other processes such as recrystallization as well as on mechanical properties (via irradiation hardening).

Declaration of competing interest

This study and the manuscript present no conflict of interest.

CRediT authorship contribution statement

V. Shah: Conceptualization, Data curation, Formal analysis, Investigation, Methodology, Software, Validation, Visualization, Writing - original draft. **J.A.W. van Dommelen:** Conceptualization, Funding acquisition, Methodology, Project administration, Supervision, Writing - review & editing. **M.G.D. Geers:** Conceptualization, Funding acquisition, Methodology, Resources, Supervision, Writing - review & editing.

Acknowledgments

This research was carried out under project number T16010c in the framework of the Research Program of the Materials innovation institute (M2i) (www.m2i.nl) supported by the Dutch government. This work has been carried out within the framework of the EUROfusion Consortium and has received funding from the Euratom research and training programme 2014–2018 and 2019–2020 under grant agreement No 633053. The views and opinions expressed herein do not necessarily reflect those of the European Commission.

Data availability

The data generated or analysed in this study are available upon reasonable request.

A Cluster dynamics model parameterization

A.1 Rate equations

Vacancy clusters (V_m):

$$\frac{\partial C_V}{\partial t} = G_V + \frac{\partial}{\partial x}\left(D_V \frac{\partial C_V}{\partial x}\right) + k^+_{I+V} C_I^{eq} C_V^{eq} + 2\gamma_2^- C_{V_2} + \sum_{n\geq 3}^{N_I} k^-_{I_{n-1}} C_{I_{n-1}} + \sum_{m=2}^{M_V-1} \gamma^-_{m+1} C_{V_{m+1}} + \sum_{m=1}^{M_V} m\delta_{resol} C_{He_nV_m} + \sum_{n=1}^{N_{He}} \sum_{m=1}^{M_V-1} \omega^-_{m+1} C_{He_nV_{m+1}}$$
$$+ \sum_{n=1}^{N_{He}} k^-_{He_nV} C_{He_nV} - k^+_{I+V} C_I C_V - k^+_{I_2+V} C_V C_{I_2} - \sum_{n\geq 3}^{N_I} k^+_{I_n+V} C_V C_{I_n} - 2\gamma_1^+ C_V^2 - \sum_{m=2}^{M_V-1} \gamma^+_m C_V C_{V_m} - \sum_{n=1}^{N_{He}} k^+_{He_n+V} C_V C_{He_n}$$
$$- \sum_{n=1}^{N_{He}} \sum_{m=1}^{M_V-1} \omega^+_m C_V C_{He_nV_m} - \sum_{n=2} k^+_{V+He_n} C_V C_{He_n} - k^+_{GB+V} C_V - k^+_{D+V} C_V$$

$$\frac{dC_{V_m}}{dt}|_{2\leq m\leq N_{V-1}} = G_{V_m} + k^+_{V_{m+1}+I} C_I C_{V_{m+1}} + k^+_{V_{m+2}+I_2} C_{I_2} C_{V_{m+2}} + \gamma^+_{m-1} C_V C_{V_{m-1}} + \gamma^-_{m+1} C_{V_{m+1}} + k^-_{HeV_m} C_{HeV_m} - k^+_{V_m+I} C_I C_{V_m}$$
$$- k^+_{V_m+I_2} C_{I_2} C_{Vm} - \gamma^+_m C_V C_{V_m} - \gamma^-_m C_{V_m} - k^+_{V_m+He} C_{He} C_{V_m} - \sum_{n=2}^{5} k^+_{V_m+He_n} C_{V_m} C_{He_n}$$

$$\frac{dC_{V_m}}{dt}|_{m=N_V} = G_{V_m} + \gamma^+_{m-1} C_V C_{V_{m-1}} + k^-_{HeV_m} C_{HeV_m} - \gamma^-_m C_{V_m} - k^+_{V_m+I} C_I C_{V_m} - k^+_{V_m+I_2} C_{I_2} C_{V_m} - k^+_{V_m+He} C_{He} C_{V_m} - \sum_{n=2}^{5} k^+_{V_m+He_n} C_{V_m} C_{He_n}$$

Self-interstitial clusters (I_n):

$$\frac{\partial C_I}{\partial t} = G_I + \frac{\partial}{\partial x}\left(D_I \frac{\partial C_I}{\partial x}\right) + 2\alpha_2^- C_{I_2} + k_{I+V}^+ C_I^{eq} C_V^{eq} + k_{V+I_2}^+ C_V C_{I_2} + \sum_{n\geq 2}^{N_I-1} \alpha_{n+1}^- C_{I_{n+1}} + \sum_{n=6}^{N_{He}} k_{ST}^- C_{He_n} + \sum_{n/m>8} k_{TM}^- C_{He_n V_m} - k_{I+V}^+ C_I C_V$$
$$- \sum_{m=2}^{M_V} k_{V_m+I}^+ C_I C_{V_m} - 2\alpha_1^+ C_I^2 - \sum_{n\geq 2}^{N_I-1} \alpha_n^+ C_I C_{I_n} - \sum_{n=1}^{N_{He}} \sum_{m=1}^{M_V} k_{He_n V_m+I}^+ C_I C_{He_n V_m} - k_{GB+I}^+ C_I - k_{D+I}^+ C_I$$

$$\frac{\partial C_{I_2}}{\partial t} = G_{I_2} + \frac{\partial}{\partial x}\left(D_{I_2} \frac{\partial C_{I_2}}{\partial x}\right) + \alpha_1^+ C_I^2 + \alpha_3^- C_{I_3} + 2\beta_4^- C_{I_4} + \sum_{n\geq 3}^{N_I-2} \beta_{n+2}^- C_{I_{n+2}} - k_{I_3+V}^+ C_{I_3} C_V - \alpha_2^- C_{I_2} - \alpha_2^+ C_{I_2} C_I - \sum_{m=1}^{M_V} k_{V_m+I_2}^+ C_{V_m} C_{I_2} - 2\beta_2^+ C_{I_2}^2$$
$$- \sum_{n\geq 3}^{N_I-2} \beta_n^+ C_{I_2} C_{I_n} - \sum_{n=1}^{N_{He}} \sum_{m=1}^{M_V} k_{He_n V_m+I_2}^+ C_{I_2} C_{He_n V_m} - k_{GB+I_2}^+ C_{I_2} - k_{D+I_2}^+ C_{I_2}$$

$$\frac{dC_{I_n}}{dt}|_{3\leq n\leq N_I-2} = G_{I_n} + \alpha_{n+1}^- C_{I_{n+1}} + \alpha_{n-1}^+ C_I C_{I_{n-1}} + \beta_{n+2}^- C_{I_{n+2}} + \beta_{n-2}^+ C_{I_2} C_{I_{n-2}} + k_{I_{n-1}+V}^- C_{I_{n-1}} + k_{I_{n+1}+V}^+ C_V C_{I_{n+1}} - \alpha_n^+ C_I C_{I_n} - \alpha_n^- C_{I_n}$$
$$- \beta_n^+ C_{I_2} C_{I_n} - \beta_n^- C_{I_n} - k_{I_n+V}^+ C_V C_{I_n} - k_{I_n+V}^- C_{I_n}$$

$$\frac{dC_{I_n}}{dt}|_{n=N_I-1} = G_{I_n} + \alpha_{n+1}^- C_{I_{n+1}} + \alpha_{n-1}^+ C_I C_{I_{n-1}} + k_{I_{n-1}+V}^- C_{I_{n-1}} + k_{I_{n+1}+V}^+ C_V C_{I_{n+1}} + \beta_{n-2}^+ C_{I_2} C_{I_{n-2}} - \alpha_n^+ C_I C_{I_n} - \alpha_n^- C_{I_n} - \beta_n^- C_{I_n}$$
$$- k_{I_n+V}^+ C_V C_{I_n} - k_{I_n+V}^- C_{I_n}$$

$$\frac{dC_{I_n}}{dt}|_{n=N_I} = G_{I_n} + \alpha_{n-1}^+ C_I C_{I_{n-1}} + \beta_{n-2}^+ C_{I_2} C_{I_{n-2}} + k_{I_{n-1}+V}^- C_{I_{n-1}} - \alpha_n^- C_{I_n} - \beta_n^- C_{I_n} - k_{I_n+V}^+ C_V C_{I_n}$$

Helium clusters (He_n):

$$\frac{\partial C_{He}}{\partial t} = G_{He} + \frac{\partial}{\partial x}\left(D_{He}\frac{\partial C_{He}}{\partial x}\right) + 2\eta_2^- C_{He_2} + \sum_{n=2}^{N_{He}-1}\eta_{n+1}^- C_{He_{n+1}} + \sum_{m=1}^{M_V} k_{HeV_m}^- C_{HeV_m} + \sum_{n=1}^{N_{He}}\sum_{m=1}^{M_V}\mu V_{(n+1)m}^- C_{He}C_{He_{n+1}V_m} + \delta_{resol}C_{He}^{GB} + \delta_{resol}C_{He}^{D}$$
$$+\zeta_{GB}^- C_{He}^{GB} + \zeta_D^- C_{He}^D + \sum_{n=2}^{N_{He}} n\delta_{resol}C_{He_n} + \sum_{n=1}^{N_{He}} n\delta_{resol}C_{He_nV_m} - 2\eta_1^+ C_{He}^2 - \sum_{n=2}^{N_{He}-1}\eta_n^+ C_{He}C_{He_n} - \sum_{m=1}^{M_V} k_{V_m+He}^+ C_{He}C_{V_m}$$
$$-\sum_{n=1}^{N_{He}}\sum_{m=1}^{M_V}\mu V_{nm}^+ C_{He}C_{He_nV_m} - \sum_{n=2}^{5}\eta_{1n}^+ C_{He}C_{He_n} - k_{GB+He}^+ C_{He} - k_{D+He}^+ C_{He}$$

$$\frac{\partial C_{He_2}}{\partial t} = \frac{\partial}{\partial x}\left(D_{He_2}\frac{\partial C_{He_2}}{\partial x}\right) + \eta_3^- C_{He_3} + \eta_1^+ C_{He}C_{He} + k_{He_2V}^- C_{He_2V} + k_{He_2V+I}^+ C_{He_2V}C_I + k_{He_2V_2+I_2}^+ C_{He_2V_2}C_{I_2} - \eta_2^+ C_{He_2}C_{He} - \eta_2^- C_{He_2}$$
$$-k_{He_2+V}^+ C_{He_2}C_V - \sum_{m=2}^{M_V} k_{He_2+V_m}^+ C_{He_2}C_{V_m} - \sum_{n=2}^{5}\eta_{2n}^+ C_{He_2}C_{He_n} - k_{GB+He_2}^+ C_{He_2} - k_{D+He_2}^+ C_{He_2} - \delta_{resol}C_{He_2}$$

$$\frac{\partial C_{He_3}}{\partial t} = \frac{\partial}{\partial x}\left(D_{He_3}\frac{\partial C_{He_3}}{\partial x}\right) + \eta_4^- C_{He_4} + \eta_2^+ C_{He}C_{He_2} + k_{He_3V}^- C_{He_3V} + k_{He_3V+I}^+ C_{He_3V}C_I$$
$$+k_{He_3V_2+I_2}^+ C_{He_3V_2}C_{I_2} + \eta_{12}^+ C_{He}C_{He_2} - \eta_3^+ C_{He_3}C_{He} - \eta_3^- C_{He_3}$$
$$-k_{He_3+V}^+ C_{He_3}C_V - \sum_{m=2}^{M_V} k_{He_3+V_m}^+ C_{He_3}C_{V_m} - \sum_{n=2}^{5}\eta_{3n}^+ C_{He_3}C_{He_n} - k_{GB+He_3}^+ C_{He_3}$$
$$-k_{D+He_3}^+ C_{He_3} - \delta_{resol}C_{He_3}$$

$$\frac{\partial C_{He_4}}{\partial t} = \frac{\partial}{\partial x}\left(D_{He_4}\frac{\partial C_{He_4}}{\partial x}\right) + \eta_5^- C_{He_5} + \eta_3^+ C_{He}C_{He_3} + k_{He_4V}^- C_{He_4V} + k_{He_4V+I}^+ C_{He_4V}C_I$$
$$+k_{He_4V_2+I_2}^+ C_{He_4V_2}C_{I_2} + \eta_{11}^+ C_{He}C_{He_3} + \eta_{22}^+ C_{He_2}^2 - \eta_4^+ C_{He_4}C_{He} - \eta_4^- C_{He_4}$$
$$-k_{He_4+V}^+ C_{He_4}C_V - \sum_{m=2}^{M_V} k_{He_4+V_m}^+ C_{He_4}C_{V_m} - \sum_{n=2}^{5}\eta_{4n}^+ C_{He_4}C_{He_n} - k_{GB+He_4}^+ C_{He_4}$$
$$-k_{D+He_4}^+ C_{He_4} - \delta_{resol}C_{He_4}$$

$$\frac{\partial C_{He_5}}{\partial t} = \frac{\partial}{\partial x}\left(D_{He_5}\frac{\partial C_{He_5}}{\partial x}\right) + \eta_6^- C_{He_6} + \eta_4^+ C_{He} C_{He_4} + k^+_{He_5V+I} C_{He_5V} C_I + k^+_{He_5V_2+I_2} C_{He_5V_2} C_{I_2} + k^-_{He_5V} C_{He_5V} + \eta^+_{23} C_{He_2} C_{He_3} + \eta^+_{32} C_{He_3} C_{He_2}$$
$$-\eta_5^+ C_{He_5} C_{He} - \eta_5^- C_{He_5} - k^+_{He_5+V} C_{He_5} C_V - \sum_{m=2}^{M_V} k^+_{He_5+V_m} C_{He_5} C_{V_m} - \sum_{n=2}^{5} \eta^+_{5n} C_{He_5} C_{He_n} - k^+_{GB+He_5} C_{He_5} - k^+_{D+He_5} C_{He_5} - \delta_{resol} C_{He_5}$$

$$\frac{dC^1_{He_n}}{dt}\Big|_{6\le n\le N_{He}} = +\eta^-_{n+1} C_{He_{n+1}} + \eta^+_{n-1} C_{He} C_{He_{n-1}} + k^-_{He_nV} C_{He_nV} + k^+_{He_nV+I} C_{He_nV} C_I + k^+_{He_nV_2+I_2} C_{He_nV_2} C_{I_2} + \left(\sum_{m=2}^{5} \eta^+_{(n-m)(m)} C_{He_{n-m}} C_{He_m}\right)$$
$$-\eta^+_n C_{He_n} C_{He_n} - \eta^-_n C_{He_n} - k^+_{He_n+V} C_{He_n} C_V - \left(\sum_{m=2}^{5} \eta^+_{nm} C_{He_n} C_{He_m}\right)_{6\le n\le N_{He}-5} - \left(\sum_{m=2}^{4} \eta^+_{nm} C_{He_n} C_{He_m}\right)_{n=N_{He}-4}$$
$$-\left(\sum_{m=2}^{3} \eta^+_{nm} C_{He_n} C_{He_m}\right)_{n=N_{He}-3} - \left(\eta^+_{nm} C_{He_n} C_{He_m}\right)_{n=N_{He}-2} - k^-_{ST} C_{He_n}|_{n>6} - \delta_{resol} C_{He_n}$$

[1]The rate coefficient for reactions with larger immobile helium clusters are evaluated as η^+_η.

Helium - Vacancy clusters (He_nV_m):

$$\left.\frac{dC_{He_nV_m}}{dt}\right|_{\substack{1\le n\le N_{He}\\ m=1}} = +\omega^-_{m+1} C_{He_nV_{m+1}} + \mu V^+_{(n-1)m} C_{He} C_{He_{n-1}V_m} + k^+_{He_nV_{m+1}+I} C_I C_{He_nV_{m+1}}$$
$$+k^+_{He_nV_{m+2}+I_2} C_{I_2} C_{He_nV_{m+2}} + \left(k^+_{V_m+He_n} C_{He_nV_m}\right)_{2\le n\le 5} + \left(k^-_{ST} C_{He_n}\right)_{n>6}$$
$$+\left(\sum_{x=2}^{5} \mu^+_{(n-x)mx} C_{He_{n-x}V_m} C_{He_x}\right)_{6\le n\le N_{He}} + \left(\sum_{x=2}^{4} \mu^+_{(n-x)mx} C_{He_{n-x}V_m} C_{He_x}\right)_{n=5}$$
$$+\left(\sum_{x=2}^{3} \mu^+_{(n-x)mx} C_{He_{n-x}V_m} C_{He_x}\right)_{n=4} + \left(\mu^+_{(1)m2} C_{He_1V_m} C_{He_2}\right)_{n=3}$$
$$+\left(\mu V^-_{(n+1)m} C_{He_{n+1}V_m}\right)_{1\le n\le N_{He}-1} - \omega^+_m C_V C_{He_nV_m} - \mu V^-_{(n)m} C_{He_nV_m}$$
$$-\left(\mu V^+_{nm} C_{He} C_{He_nV_m}\right)_{1\le n\le N_{He}-1} - k^+_{He_nV_m+I} C_I C_{He_nV_m} - k^+_{He_nV_m+I_2} C_{I_2} C_{He_nV_m}$$
$$-\left(k^-_{TM} C_{He_nV_m}\right)_{n/m>8} - \left(\sum_{x=2}^{5} \mu^+_{(nm)x} C_{He_nV_m} C_{He_x}\right)_{n\le N_{He}-5}$$
$$-\left(\sum_{x=2}^{4} \mu^+_{(nm)x} C_{He_nV_m} C_{He_x}\right)_{n=N_{He}-4} - \left(\sum_{x=2}^{3} \mu^+_{(nm)x} C_{He_nV_m} C_{He_x}\right)_{n=N_{He}-3}$$
$$-\left(\mu^+_{(nm)2} C_{He_nV_m} C_{He_2}\right)_{n=N_{He}-2} - \delta_{resol} C_{He_nV_m}$$

$$\frac{dC_{He_nV_m}}{dt}\Big|\ 1 \le n \le N_{He} \quad 2 \le m \le M_V = +\omega^+_{m-1}C_V C_{He_nV_{m-1}} + \mu V^+_{(n-1)m} C_{He} C_{V_m} + \left(\omega^-_{m+1} C_{He_nV_{m+1}}\right)_{2\le m\le M_V-1}$$

$$+\left(\mu V^-_{(n+1)m} C_{He_{n+1}V_m}\right)_{2\le n\le N_{He}-1} + \left(k^+_{He_nV_{m+1}+I} C_I C_{He_nV_{m+1}}\right)_{2\le m\le M_V-1}$$

$$+\left(k^+_{He_nV_{m+2}+I_2} C_{I_2} C_{He_nV_{m+2}}\right)_{2\le m\le M_V-2} + \left(k^+_{V_m+He_n} C_{He_nV_m}\right)_{2\le n\le 5}$$

$$+\left(\sum_{x=2}^{5} \mu^+_{(n-x)mx} C_{He_{n-x}V_m} C_{He_x}\right)_{6\le n\le N_{He}} + \left(\sum_{x=2}^{4} \mu^+_{(n-x)mx} C_{He_{n-x}V_m} C_{He_x}\right)_{n=5}$$

$$+\left(\sum_{x=2}^{3} \mu^+_{(n-x)mx} C_{He_{n-x}V_m} C_{He_x}\right)_{n=4} + \left(\mu^+_{(1)m2} C_{He_1V_m} C_{He_2}\right)_{n=3}$$

$$+\left(k^-_{TM} C_{He_nV_{m-1}}\right)_{n/m>8} - \left(\omega^+_m C_V C_{He_nV_m}\right)_{2\le m\le M_V-1} - \omega^-_m C_{He_nV_m}$$

$$-\left(\mu V^+_{(n)m} C_{He} C_{He_nV_m}\right)_{2\le n\le N_{He}-1} - \mu V^-_{(n)m} C_{He_nV_m}$$

$$-k^+_{He_nV_m+I} C_I C_{He_nV_m} - k^+_{He_nV_m+I_2} C_{I_2} C_{He_nV_m} - \left(k^-_{TM} C_{He_nV_m}\right)_{n/m>8}$$

$$-\left(\sum_{x=2}^{5} \mu^+_{(nm)x} C_{He_nV_m} C_{He_x}\right)_{n\le N_{He}-5} - \left(\sum_{x=2}^{4} \mu^+_{(nm)x} C_{He_nV_m} C_{He_x}\right)_{n=N_{He}-4}$$

$$-\left(\sum_{x=2}^{3} \mu^+_{(nm)x} C_{He_nV_m} C_{He_x}\right)_{n=N_{He}-3} - \left(\mu^+_{(nm)2} C_{He_nV_m} C_{He_2}\right)_{n=N_{He}-2}$$

$$-\delta_{resol} C_{He_nV_m}$$

A.2 Interaction reactions

Table 2
Interaction reactions between different defects and the associated rate coefficients, adapted from [27,57,60,105].

#	Reaction	Rate coefficients
1	$I + V \rightarrow 0$	k^+_{I+V}
2	$I_n + I \rightleftharpoons I_{n+1}$	α^+_n, α^-_{n+1}
3	$V_m + I \rightarrow V_{m-1}$	$k^+_{V_m+I}$
4	$He_nV_m + I \rightarrow He_nV_{m-1}$	$k^+_{He_nV_m+I}$
5	$I_n + I_2 \rightleftharpoons I_{n+2}$	β^+_n, β^-_{n+2}
6	$V_m + I_2 \rightarrow V_{m-2}$	$k^+_{V_m+I_2}$
7	$He_nV_m + I_2 \rightarrow He_nV_{m-2}$	$k^+_{He_nV_m+I_2}$
8	$I_n + V \rightarrow I_{n-1}$	$k^+_{I_n+V}$, $k^-_{I_{n-1}+V}$
9	$V_m + V \rightleftharpoons V_{m+1}$	γ^+_m, γ^-_{m+1}
10	$He_n + V \rightleftharpoons He_nV$	$k^+_{He_n+V}$, $k^-_{He_nV}$
11	$He_nV_m + V \rightleftharpoons He_nV_{m+1}$	ω^+_m, ω^-_{m+1}
12	$V_m + He \rightleftharpoons HeV_m$	$k^+_{V_m+He}$, $k^-_{HeV_m}$
13	$He_n + He \rightleftharpoons He_{n+1}$	η^+_n, η^-_{n+1}
14	$He_nV_m + He \rightleftharpoons He_{n+1}V_m$	μV^+_{nm}, $\mu V^-_{(n+1)m}$
15	$He_n \xrightarrow{ST} He_nV + I$ [1]	k^-_{ST} $(n \ge 6)$
16	$He_nV_m \xrightarrow{TM} He_nV_{m+1} + I$ [1]	k^-_{TM} $(n/m$ ratio $\ge 8)$
17	$He_{m-n} + He_n \rightarrow He_m$	$\eta^+_{(m-n)n}$ $(2 \le n \le 5,$ $m = [n+1]\ldots N_{He})$
18	$V_m + He_n \rightarrow He_nV_m$	$k^+_{V_m+He_n}$ $(2 \le n \le 5,$ $m = 1\ldots N_V)$
19	$He_{n-x}V_m + He_x \rightarrow He_nV_m$	$\mu V^+_{(n-x)mx}$ $(2 \le x \le 5,$

(continued on next page)

Table 2 (*continued*)

#	Reaction	Rate coefficients
		$n = [x+1]...M_{He}$, $m = 1...N_V$)
20	$D + \theta \rightarrow \theta_D$ [2]	$k^+_{D+\theta}$ $(\theta \rightarrow V, I, I_2)$
21	$D + \theta' \rightarrow \theta'_D$	$k^+_{D+\theta'}$ $(\theta' \rightarrow He_n, 1 \leq n \leq 5)$
22	$GB + \theta \rightarrow \theta_{GB}$ [2]	$k^+_{GB+\theta}$ $(\theta \rightarrow V, I, I_2)$
23	$GB + \theta' \rightarrow \theta'_{GB}$	$k^+_{GB+\theta'}$ $(\theta' \rightarrow He_n, 1 \leq n \leq 5)$
24	$He_{GB}/He_D \xrightarrow{detrapping} He$	$\zeta_{GB/D}$
25	$He_{GB}/He_D \xrightarrow{resolution} He$	δ_{resol}
26	$He_n \xrightarrow{resolution} nHe$	δ_{resol}
27	$He_nV_m \xrightarrow{resolution} nHe + mV$	δ_{resol}

[1] ST denotes self-trapping and TM denotes trap-mutation.
[2] D denotes dislocations and GB denotes grain boundaries.

A.3 Rate coefficients

A.3.1 Defect clusters

Table 3
Expression for the trapping and detrapping rate of the interaction reactions between different defects.

Reaction	Trapping rate	Detrapping rate	Mobile species
Vacancy clusters (V_m)			
$V_m - I$	$k^+_{V_m+I} = 4\pi r_{V_m} D_I$	–	I
$V_m - I_2$	$k^+_{V_m+I_2} = 4\pi r_{V_m} D_{I_2}$	–	I_2
$V_m - V$	$\gamma^+_m = 4\pi r_{V_m} D_V$	$\gamma^-_{m+1} = \gamma^+ \exp(-E^b_{V_m-V}/k_BT)/\Omega$	V
$V_m - He$	$k^+_{V_m+He} = 4\pi r_{V_m} D_{He}$	$k^-_{HeV_m} = k^+_{V_m+He} \exp(-E^b_{V_m-He}/k_BT)/\Omega$	He
$V_m - He_n$	$k^+_{V_m+He_n} = 4\pi r_{V_m} D_{He_n}$	–	He_n, $2 \leq n \leq 5$
SIA loops (I_n)			
$I_n - I$	$\alpha^+_n = 2\pi r_{I_n} Z^{I_n}_I D_I$	$\alpha^-_{n+1} = \alpha^+_n \exp(-E^b_{I_n-I}/k_BT)/\Omega$	I
$I_n - I_2$	$\beta^+_n = 2\pi r_{I_n} Z^{I_n}_{I_2} D_{I_2}$	$\beta^-_{n+2} = \beta^+_n \exp(-E^b_{I_n-I_2}/k_BT)/\Omega$	I_2
$I_n - V$	$k^+_{I_n-V} = 2\pi r_{I_n} Z^{I_n}_V D_V$	$k^+_{I_{n-1}-V} = k^+_{I_n-V} \exp(-E^b_{I_n-V}/k_BT)/\Omega$	V
Helium clusters (He_n)			
He_n - V	$k^+_{He_n-V} = 4\pi r_{He_n} D_V$	$k^-_{He_nV} = k^+_{He_n} \exp(-E^b_{He_n-V}/k_BT)/\Omega$	V
He_n - He	$\eta^+_n = 4\pi r_{He_n} D_{He}$	$\eta^-_{n+1} = \eta^+_n \exp(-E^b_{He_n-He}/k_BT)/\Omega$	He
He_{n-x} - He_x	$\eta^+_{(n-x)x} = 4\pi r_{He_{n-x}} D_{He_x}$	–	He_x, $2 \leq x \leq 5$, $(n-x) > 5$
He^{ST}_n	–	$k^-_{ST} = 4\pi r_{He_n} D_I \exp(-E^{ST}_n/k_BT)/\Omega$	I
Helium-Vacancy clusters (He_nV_m)			
He_nV_m - I	$k^+_{He_nV_m-I} = 4\pi r_{V_m} D_I$	–	I
He_nV_m - I_2	$k^+_{He_nV_m-I_2} = 4\pi r_{V_m} D_{I_2}$	–	I_2
He_nV_m - V	$\omega^+_m = 4\pi r_{V_m} D_V$	$\omega^-_{m+1} = \omega^+_m \exp(-E^b_{He_nV_m-V}/k_BT)/\Omega$	V
He_nV_m - He	$\mu^+_{nm} = 4\pi r_{V_m} D_{He}$	$\mu^-_{(n+1)m} = \mu^+_{nm} \exp(-E^b_{He_nV_m-He}/k_BT)/\Omega$	He
$He_{n-x}V_m$ - He_x	$\mu^+_{(n-x)mx} = 4\pi r_{V_m} D_{He_x}$	–	He_x, $2 \leq x \leq 5$
$He_nV^{TM}_m$	–	$k^-_{TM} = 4\pi r_{V_m} D_I \exp(-E^{TM}_{n/m}/k_BT)/\Omega$	I
Recombination of Frenkel pair			
$I - V$	$k^+_{I+V} = 4\pi r_{IV}(D_I + D_V)$		I, V
Reaction of mobile helium clusters			
He_{n-x} - He_x	$\eta^+_{(n-x)x} = 4\pi(r_{He_{n-x}} + r_{He_x})(D_{He_{n-x}} + D_{He_x})$		$(n-x) \leq 5$, $2 \leq x \leq 5$

A.3.2 Microstructural sinks

Table 4
Expression for the trapping rate of the mobile defects at the microstructural sinks.

Reaction	Trapping rate	Matrix sink strength	Mobile species
$GB-I$	$k^+_{GB-I} = f(S^m_I)D_I$	$S^m_I = D_I^{-1}[\sum_{n=1}^{N_I-1}\alpha^+_n C_{I_n} + \sum_{m=1}^{M_V} k^+_{V_m+I} C_{V_m} + \sum_{n=1}^{N_{He}}\sum_{m=1}^{M_V} k^+_{He_nV_m+I} C_{He_nV_m}]$	I
$GB-I_2$	$k^+_{GB-I_2} = f(S^m_{I_2})D_{I_2}$	$S^m_{I_2} = D_{I_2}^{-1}[\sum_{n=1}^{N_I-2}\beta_n C_{I_n} + \sum_{m=1}^{M_V} k^+_{V_m+I_2} C_{V_m} + \sum_{n=1}^{N_{He}}\sum_{m=1}^{M_V} k^+_{He_nV_m+I_2} C_{He_nV_m}]$	I_2
$GB-V$	$k^+_{GB-V} = f(S^m_V)D_V$	$S^m_V = D_V^{-1}[\sum_{n=1}^{N_I} k^+_{I_n+V} C_{I_n} + \sum_{m=1}^{M_V-1}\gamma^+_m C_{V_m} + \sum_{n=1}^{N_{He}} k^+_{He_n+V} C_{He_n} + \sum_{n=1}^{N_{He}}\sum_{m=1}^{M_V-1}\omega^+_m C_{He_nV_m}]$	V
$GB-He$	$k^+_{GB-He} = f(S^m_{He})D_{He}$	$S^m_{He} = D_{He}^{-1}[\sum_{m=1}^{M_V} k^+_{V_m+He} C_{V_m} + \sum_{n=1}^{N_{He}-1}\eta^+_n C_{He_n} + \sum_{n=1}^{N_{He}-1}\sum_{m=1}^{M_V}\mu^+_{nm} C_{He_nV_m}]$	He
$GB-He_x$, $2 \le x \le 5$	$k^+_{GB-He_x} = f\left(S^m_{He_x}\right)D_{He_x}$	$S^m_{He_x} = D_{He_x}^{-1}\left[\sum_{m=1}^{M_V} k^+_{V_m+He_x} C_{V_m} + \sum_{n=1}^{N_{He}-x}\eta^+_n C_{He_n} + \sum_{n=1}^{N_{He}-x}\sum_{m=1}^{M_V}\mu^+_{nmx} C_{He_nV_m}\right]$	He_x
$D-I$	$k^+_{D-I} = \rho_n Z^D_I D_I$	–	I
$D-I_2$	$k^+_{D-I_2} = \rho_n Z^D_{I_2} D_{I_2}$	–	I_2
$D-V$	$k^+_{D-V} = \rho_n Z^D_V D_V$	–	He
$D-He_x$ $2 \le x \le 5$	$k^+_{D-He_x} = \rho_n Z^D_{He_x} D_{He_x}$	–	He_x

A.4 Binding energy relations

Table 5
Binding energy relationship between the defects, based on the capillary approximation and the DFT, MD simulations [57,60,82–84].

#	Reaction	Binding energy relation [eV]
1	$I_n - I$	$E^b_{I_n-I} = E^f_I + \frac{E^b_{I_2} - E^f_I}{2^{2/3}-1}[n^{2/3} - (n-1)^{2/3}]$
2	$I_n - I_2$	$E^b_{I_n-I_2} = E^b_{I_n-I} + E^b_{I_{n-1}-I} - E^b_{I_2}$
3	$I_n - V$	$E^b_{I_n-V} = E^f_V + \frac{E^f_I - E^b_{I_2}}{2^{2/3}-1}[n^{2/3} - (n-1)^{2/3}]$
4	$V_m - V$	$E^b_{V_m-V} = E^f_V + \frac{E^b_{V_2} - E^f_V}{2^{2/3}-1}[m^{2/3} - (m-1)^{2/3}]$
5	He–He	$E^b_{He_n-He} = E^f_{He} + \frac{E^b_{He_2} - E^f_{He}}{2^{2/3}-1}[n^{2/3} - (n-1)^{2/3}]$
6	He_nV_m - He	$E^b_{He_nV_m-He} = 0.015(n/m)^2 - 0.36(n/m) + 4.76$
7	He_nV_m - V	$E^b_{He_nV_m-V} = -0.14(n/m)^2 + 2.55(n/m) - 0.82$
8	$He_n \xrightarrow{ST} He_nV + I$	$E^b_{ST} = 0.002(n)^4 - 0.011n^3 + 0.227n^2 - 2.158n + 7.1803$
9	$He_nV_m \xrightarrow{TM} He_nV_{m+1} + I$	$E^b_{TM} = 0.0006(n/m)^3 - 0.0244(n/m)^2 + 0.1551(n/m) + 0.9190$

Table 6
Formation and binding energy of the defect species, used to derive the binding energies for larger clusters in Table 5.

Defect type, θ	Formation energy, E^f_θ [eV]	Binding energy, E^b_θ [eV]	Reference
V	3.80	–	Ahlgren et al. [90]
I	9.46	–	Olsson [91]
He	4.00	–	Becquart et al. [84]
V_2	–	0.65	Ahlgren et al. [90]
I_2	–	2.12	Becquart et al. [84]
He_2	–	1.02	Becquart et al. [84]

A.5 Diffusivity of mobile defects

Table 7
Migration energy and diffusion pre-exponential factors of mobile defects, used to determine the temperature dependent diffusivity.

Defect type, θ	Migration energy, E_θ^m [eV]	Pre-exponential factor, D_θ^0 [m^2s^{-1}]	Reference
V	1.66	177×10^{-8}	Becquart et al. [84]
I	0.013	8.77×10^{-8}	Becquart et al. [84]
I_2	0.024	7.97×10^{-8}	Faney et al. [27]
He	0.06	2.95×10^{-8}	Becquart et al. [84]
He_2	0.2	3.24×10^{-8}	Faney et al. [27]
He_3	0.25	2.26×10^{-8}	Faney et al. [27]
He_4	0.2	1.68×10^{-8}	Faney et al. [27]
He_5	0.12	0.52×10^{-8}	Faney et al. [27]

Table 8
Temperature dependent diffusivity of mobile defects, based on the parameters from Table 7.

Diffusivity	Equation
D_I	$D_I = D_I^0 \exp(-E_I^m/k_BT)$
D_V	$D_V = D_V^0 \exp(-E_V^m/k_BT)$
D_{He}	$D_{He} = D_{He}^0 \exp(-E_{He}^m/k_BT)$
D_{He_2}	$D_{He_2} = D_{He_2}^0 \exp(-E_{He_2}^m/k_BT)$
D_{He_3}	$D_{He_3} = D_{He_3}^0 \exp(-E_{He_3}^m/k_BT)$
D_{He_4}	$D_{He_4} = D_{He_4}^0 \exp(-E_{He_4}^m/k_BT)$
D_{He_5}	$D_{He_5} = D_{He_5}^0 \exp(-E_{He_5}^m/k_BT)$

A.6 Simulation parameters

Table 9
Simulation parameters used in the spatially dependent cluster dynamics model.

Parameter	Symbol	Value	Unit	Reference
Lattice parameter	a_0	0.316	nm	Lassner and Schubert [124]
Atomic volume	Ω	$a_0^3/2$	nm^3	Li et al. [57,60]
Burgers vector	b	0.274	nm	Li et al. [57,60]
Boltzmann's constant	k	8.617×10^{-5}	$eV\ K^{-1}$	
Atomic weight	M	183.84	$g\ mol^{-1}$	Lassner and Schubert [124]
Mass density	ρ_{at}	19.25×10^6	$g\ m^{-3}$	Lassner and Schubert [124]
Shear Modulus	μ	161×10^9	Nm^{-2}	
Atomic density	N_{at}	6.30×10^{28}	atoms m^{-3}	
Radius of Helium atom	r_{He}	0.30	nm	Faney and Wirth [76]
Helium vibrational frequency	ν_{He}	6×10^{10}	s^{-1}	Becquart et al. [84]
Recombination radius (I–V)	r_{IV}	0.465	nm	Li et al. [57,60]
Maximum V cluster size	M_V	15	–	
Maximum I cluster size	N_I	15	–	
Maximum He cluster size	N_{He}	15	–	
Number of nodes	N_x	50	–	
Irradiation time	t_{irr}	1000	hours	
He ion flux	ϕ_{He}	1×10^{22}	ions $m^{-2}s^{-1}$	Federici et al. [6]
He ion energy	E_{He}	100	eV	Iwakiri et al. [32]
Initial network - dislocation density	ρ_{init}	10^{12}	m^{-2}	
Pinned dislocation density	ρ_p	$0.05 \times \rho_n$	m^{-2}	
Grain size	d	3	μm	
Capture efficiency factor				
SIA loop - I	$Z_I^{l_n}$	1.2	–	Li et al. [57]
SIA loop - I_2	$Z_{I_2}^{l_n}$	1.2	–	Li et al. [57]
SIA loop - V	$Z_V^{l_n}$	1.0	–	Li et al. [57]
Dislocation line - I	Z_I^D	1.2	–	Li et al. [57]
Dislocation line - I_2	$Z_{I_2}^D$	1.2	–	Li et al. [57]
Dislocation line - V	Z_V^D	1.0	–	Li et al. [57]
Dislocation line - He_x $1 \leq x \leq 5$	$Z_{He_x}^D$	1.0	–	Xu et al. [125]

B FEM: Temperature profile

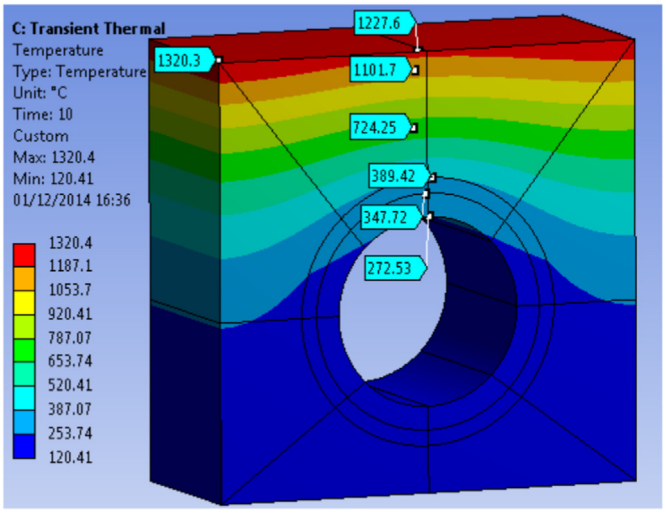

Fig. 17. Temperature distribution in the monoblock considering the steady state heat load of 10 MWm^{-2}, simulated using the ANSYS FEM platform by Panayotis et al. [120]. The surface temperature is in the range 1230°C (monoblock center) - 1320°C (monoblock edge). The estimated one dimensional temperature profile used in the current simulations corresponds to the center of the monoblock. (For interpretation of the references to colour in this figure legend, the reader is referred to the web version of this article.)

References

[1] M. Samaras, Multiscale modelling: the role of helium in iron, Mater. Today 12 (2009) 46–53, https://doi.org/10.1016/S1369-7021(09)70298-6.

[2] A.W. Kleyn, N.J. Lopes Cardozo, U. Samm, Plasma–surface interaction in the context of iter, Phys. Chem. Chem. Phys. 8 (2006) 1761–1774, https://doi.org/10.1039/B514367E.

[3] T. Hirai, F. Escourbiac, S. Carpentier-Chouchana, A. Fedosov, L. Ferrand, T. Jokinen, V. Komarov, A. Kukushkin, M. Merola, R. Mitteau, et al., ITER tungsten divertor design development and qualification program, Fusion Eng. Des. 88 (2013) 1798–1801, https://doi.org/10.1016/j.fusengdes.2013.05.010.

[4] V. Philipps, Tungsten as material for plasma-facing components in fusion devices, J. Nucl. Mater. 415 (S2–S9) (2011), https://doi.org/10.1016/j.jnucmat.2011.01.110.

[5] R.A. Pitts, S. Carpentier, F. Escourbiac, T. Hirai, V. Komarov, S. Lisgo, A.S. Kukushkin, A. Loarte, M. Merola, A.S. Naik, et al., A full tungsten divertor for ITER: physics issues and design status, J. Nucl. Mater. 438 (2013) S48–S56, https://doi.org/10.1016/j.jnucmat.2013.01.008.

[6] G. Federici, et al., Plasma-material interactions in current tokamaks and their implications for next step fusion reactors, Nucl. Fusion 41 (1967), https://doi.org/10.1088/0029-5515/41/12/218, 2001.

[7] M. Merola, G. Vieider, M. Bet, L. Vastra, I.B. Briottet, P. Chappuis, K. Cheyne, G. Dell'Orco, D. Duglue, R. Duwe, et al., European achievements for ITER high heat flux components, Fusion Eng. Des. 56 (2001) 173–178, https://doi.org/10.1016/S0920-3796(01)00253-8.

[8] A. Hasegawa, M. Fukuda, S. Nogami, K. Yabuuchi, Neutron irradiation effects on tungsten materials, Fusion Eng. Des. 89 (2014) 1568–1572, https://doi.org/10.1016/j.fusengdes.2014.04.035.

[9] J.C. He, G.Y. Tang, A. Hasegawa, K. Abe, Microstructural development and irradiation hardening of W and W–(3–26) wt% Re alloys after high-temperature neutron irradiation to 0.15 dpa, Nucl. Fusion 46 (2006) 877, https://doi.org/10.1088/0029-5515/46/11/001.

[10] M.R. Gilbert, J.-Ch Sublet, Neutron-induced transmutation effects in W and W-alloys in a fusion environment, Nucl. Fusion 51 (2011), https://doi.org/10.1088/0029-5515/51/4/043005, 043005.

[11] T. Tanno, A. Hasegawa, J.-C. He, M. Fujiwara, S. Nogami, M. Satou, T. Shishido, K. Abe, Effects of transmutation elements on neutron irradiation hardening of tungsten, Mater. Trans. 48 (2007) 2399–2402, https://doi.org/10.2320/matertrans.MAW200722.

[12] T. Tanno, A. Hasegawa, M. Fujiwara, J.-Ch He, S. Nogami, M. Satou, T. Shishido, K. Abe, Precipitation of solid transmutation elements in irradiated tungsten alloys, Mater. Trans. 49 (2008) 2259–2264, https://doi.org/10.2320/matertrans.MAW200821.

[13] F. Haessner, H.P. Holzer, Boundary migration in neutron-irradiated copper bicrystals, Scripta Metall. 4 (1970) 161–165, https://doi.org/10.1016/0036-9748(70)90185-7.

[14] F. Haessner, H.P. Holzer, The effect of fast neutron irradiation on the recrystallization of cold-rolled (110)[112] oriented copper crystals, Acta Metall. 22 (1974) 695–708, https://doi.org/10.1016/0001-6160(74)90079-0.

[15] W.V. Vaidya, K. Ehrlich, Radiation-induced recrystallization, its cause and consequences in heavy-ion irradiated 20% cold-drawn steels of type 1.4970, J. Nucl. Mater. 113 (1983) 149–162, https://doi.org/10.1016/0022-3115(83)90137-X.

[16] P. Wang, D.A. Thompson, W.W. Smeltzer, Implantation of Ni thin films and single crystals with Ag ions, Nucl. Instrum. Methods Phys. Res. Sect. B Beam Interact. Mater. Atoms 7 (1985) 97–102, https://doi.org/10.1016/0168-583X(85)90536-1.

[17] H.A. Atwater, C.V. Thompson, H.I. Smith, Ion-bombardment-enhanced grain growth in germanium, silicon, and gold thin films, J. Appl. Phys. 64 (1988) 2337–2353, https://doi.org/10.1063/1.341665.

[18] A. Mannheim, J.A.W. van Dommelen, M.G.D. Geers, Modelling recrystallization and grain growth of tungsten induced by neutron displacement defects, Mech. Mater. 123 (2018) 43–58, https://doi.org/10.1016/j.mechmat.2018.04.008.

[19] W.R. Wampler, R.P. Doerner, The influence of displacement damage on deuterium retention in tungsten exposed to plasma, Nucl. Fusion 49 (2009), 115023, https://doi.org/10.1088/0029-5515/49/11/115023.

[20] G.M. Wright, M. Mayer, K. Ertl, G. de Saint-Aubin, J. Rapp, Hydrogenic retention in irradiated tungsten exposed to high-flux plasma, Nucl. Fusion 50 (2010), 075006, https://doi.org/10.1088/0029-5515/50/7/075006.

[21] S. Markelj, T. Schwarz-Selinger, A. Založnik, Hydrogen isotope accumulation in the helium implantation zone in tungsten, Nucl. Fusion 57 (2017), 064002, https://doi.org/10.1088/1741-4326/aa6b27.

[22] A.S. Soltan, R. Vassen, P. Jung, Migration and immobilization of hydrogen and helium in gold and tungsten at low temperatures, J. Appl. Phys. 70 (1991) 793–797, https://doi.org/10.1063/1.349636.

[23] C.S. Becquart, C. Domain, Migration energy of He in W revisited by ab initio calculations, Phys. Rev. Lett. 97 (2006), 196402, https://doi.org/10.1103/PhysRevLett.97.196402.

[24] V. Borovikov, A.F. Voter, X.-Z. Tang, Reflection and implantation of low energy helium with tungsten surfaces, J. Nucl. Mater. 447 (1–3) (2014) 254–270, https://doi.org/10.1016/j.jnucmat.2014.01.021.

[25] M.S.A. El Keriem, D.P. Van Der Werf, F. Pleiter, Helium-vacancy interaction in tungsten, Phys. Rev. B 47 (1993), 14771, https://doi.org/10.1103/PhysRevB.47.14771.

[26] C.S. Becquart, C. Domain, Solute–point defect interactions in bcc systems: focus on first principles modelling in W and RPV steels, Curr. Opin. Solid State Mater. Sci. 16 (3) (2012) 115–125, https://doi.org/10.1016/j.cossms.2012.01.001.

[27] T. Faney, S.I. Krasheninnikov, B.D. Wirth, Spatially dependent cluster dynamics model of He plasma surface interaction in tungsten for fusion relevant conditions, Nucl. Fusion 55 (2015), 013014, https://doi.org/10.1088/0029-5515/55/1/013014.

[28] X.-C. Li, X. Shu, P. Tao, Y. Yu, G.-J. Niu, Y. Xu, F. Gao, G.-N. Luo, Molecular dynamics simulation of helium cluster diffusion and bubble formation in bulk tungsten, J. Nucl. Mater. 455 (2014) 544–548, https://doi.org/10.1016/j.jnucmat.2014.08.028.

[29] Y.L. Zhou, J. Wang, Q. Hou, A.H. Deng, Molecular dynamics simulations of the diffusion and coalescence of helium in tungsten, J. Nucl. Mater. 446 (2014) 49–55, https://doi.org/10.1016/j.jnucmat.2013.11.034.

[30] D. Perez, T. Vogel, B.P. Uberuaga, Diffusion and transformation kinetics of small helium clusters in bulk tungsten, Phys. Rev. B 90 (2014), 014102, https://doi.org/10.1103/PhysRevB.90.014102.

[31] R.J.K. Nicholson, J.M. Walls, FIM studies of the lattice damage in tungsten following low-energy helium ion bombardment, J. Nucl. Mater. 76 (1978) 251–252, https://doi.org/10.1016/0022-3115(78)90150-2.

[32] H. Iwakiri, K. Yasunaga, K. Morishita, N. Yoshida, Microstructure evolution in tungsten during low-energy helium ion irradiation, J. Nucl. Mater. 283 (2000) 1134–1138, https://doi.org/10.1016/S0022-3115(00)00289-0.

[33] K.O.E. Henriksson, K. Nordlund, J. Keinonen, Molecular dynamics simulations of helium cluster formation in tungsten, Nucl. Instrum. Methods Phys. Res. Sect. B Beam Interact. Mater. Atoms 244 (2006) 377–391, https://doi.org/10.1016/j.nimb.2005.10.020.

[34] W. Kesternich, Helium trapping at dislocations, precipitates and grain boundaries, Radiat. Eff. 78 (1983) 261–273, https://doi.org/10.1080/00337578308207376.

[35] B.N. Singh, T. Leffers, W.V. Green, M. Victoria, Nucleation of helium bubbles on dislocations, dislocation networks and dislocations in grain boundaries during 600 MeV proton irradiation of aluminium, J. Nucl. Mater. 125 (1984) 287–297, https://doi.org/10.1016/0022-3115(84)90556-7.

[36] P.A. Thorsen, J.B. Bilde-Sørensen, B.N. Singh, Bubble formation at grain boundaries in helium implanted copper, Scripta Mater. 51 (2004) 557–560, https://doi.org/10.1016/j.scriptamat.2004.05.038.

[37] O. El-Atwani, S. Gonderman, M. Efe, G. De Temmerman, T. Morgan, K. Bystrov, D. Klenosky, T. Qiu, J.P. Allain, Ultrafine tungsten as a plasma-facing component in fusion devices: effect of high flux, high fluence low energy helium irradiation, Nucl. Fusion 54 (2014), 083013, https://doi.org/10.1088/0029-5515/54/8/083013.

[38] K. Chockalingam, P.C. Millett, M.R. Tonks, Effects of intergranular gas bubbles on thermal conductivity, J. Nucl. Mater. 430 (2012) 166–170, https://doi.org/10.1016/j.jnucmat.2012.06.027.
[39] Y.M. Aleksandrova, L.N. Aleksandrov, V.D. Eliséeva, Effect of inert gases on the recrystallization of tungsten, Mater. Sci. 2 (1967) 234–237, https://doi.org/10.1007/BF00714677.
[40] K. Farrell, A.C. Schaffhauser, J.T. Houston, Effect of gas bubbles on recrystallization of tungsten, Metall. Trans. 1 (1970) 2899–2905, https://doi.org/10.1007/BF03037829.
[41] R. Nagasaki, S. Ohashi, S. Kawasaki, Y. Karita, N. Tsuno, Behavior of helium gas bubbles in neutron-irradiated beryllium, J. Nucl. Sci. Technol. 8 (10) (1971) 546–552, https://doi.org/10.1080/18811248.1971.9732995.
[42] W. Guo, L. Cheng, G. De Temmerman, Y. Yuan, G.-H. Lu, Retarded recrystallization of helium-exposed tungsten, Nucl. Fusion 58 (2018), 106011, https://doi.org/10.1088/1741-4326/aad2b0.
[43] O. El-Atwani, K. Hattar, J.A. Hinks, G. Greaves, S.S. Harilal, A. Hassanein, Helium bubble formation in ultrafine and nanocrystalline tungsten under different extreme conditions, J. Nucl. Mater. 458 (2015) 216–223, https://doi.org/10.1016/j.jnucmat.2014.12.095.
[44] K. Wang, M.E. Bannister, F.W. Meyer, C.M. Parish, Effect of starting microstructure on helium plasma-materials interaction in tungsten, Acta Mater. 124 (2017) 556–567, https://doi.org/10.1016/j.actamat.2016.11.042.
[45] V. Shah, M.P.F.H.L. van Maris, J.A.W. van Dommelen, M.G.D. Geers, Experimental investigation of the microstructural changes of tungsten monoblocks exposed to pulsed high heat loads, Nuclear Materials and Energy 22 (2020), 100716. https://doi.org/10.1016/j.nme.2019.100716.
[46] H. Trinkaus, Modeling of helium effects in metals: high temperature embrittlement, J. Nucl. Mater. 133 (1985) 105–112, https://doi.org/10.1016/0022-3115(85)90119-9.
[47] V.I. Gerasimenko, I.M. Mikhailovskii, I.M. Neklyudov, A.A. Parkhomenko, O.A. Velikodnaya, Changes in the fine structure of grain boundaries, induced by the absorption of helium, and helium embrittlement, Tech. Phys. 43 (1998) 803–808, https://doi.org/10.1134/1.1259076.
[48] M.R. Gilbert, S.L. Dudarev, D. Nguyen-Manh, S. Zheng, L.W. Packer, J.-Ch Sublet, Neutron-induced dpa, transmutations, gas production, and helium embrittlement of fusion materials, J. Nucl. Mater. 442 (2013) S755–S760, https://doi.org/10.1016/j.jnucmat.2013.03.085.
[49] K. Nordlund, C. Björkas, T. Ahlgren, A. Lasa, A.E. Sand, Multiscale modelling of plasma–wall interactions in fusion reactor conditions, J. Phys. Appl. Phys. 47 (22) (2014), 224018, https://doi.org/10.1016/j.nimb.2012.10.038.
[50] R.E. Stoller, S.I. Golubov, C. Domain, C.S. Becquart, Mean field rate theory and object kinetic Monte Carlo: a comparison of kinetic models, J. Nucl. Mater. 382 (2008) 77–90, https://doi.org/10.1016/j.jnucmat.2008.08.047.
[51] S.I. Golubov, A.M. Ovcharenko, A.V. Barashev, B.N. Singh, Grouping method for the approximate solution of a kinetic equation describing the evolution of point-defect clusters, Philos. Mag. A 81 (2001) 643–658, https://doi.org/10.1080/01418610108212164.
[52] J. Marian, V.V. Bulatov, Stochastic cluster dynamics method for simulations of multispecies irradiation damage accumulation, J. Nucl. Mater. 415 (2011) 84–95, https://doi.org/10.1016/j.jnucmat.2011.05.045.
[53] T. Jourdan, G. Bencteux, G. Adjanor, Efficient simulation of kinetics of radiation induced defects: a cluster dynamics approach, J. Nucl. Mater. 444 (2014) 298–313, https://doi.org/10.1016/j.jnucmat.2013.10.009.
[54] A.A. Kohnert, B.D. Wirth, Grouping techniques for large-scale cluster dynamics simulations of reaction diffusion processes, Model. Simulat. Mater. Sci. Eng. 25 (2016), 015008, https://doi.org/10.1088/1361-651X/25/1/015008.
[55] C.S. Becquart, C. Domain, An object kinetic Monte Carlo simulation of the dynamics of helium and point defects in tungsten, J. Nucl. Mater. 385 (2009) 223–227, https://doi.org/10.1016/j.jnucmat.2008.11.027.
[56] A. Rivera, G. Valles, M.J. Caturla, I. Martin-Bragado, Effect of ion flux on helium retention in helium-irradiated tungsten, Nucl. Instrum. Methods Phys. Res. Sect. B Beam Interact. Mater. Atoms 303 (2013) 81–83, https://doi.org/10.1016/j.nimb.2012.10.038.
[57] Y.G. Li, W.H. Zhou, R.H. Ning, L.F. Huang, Z. Zeng, X. Ju, A cluster dynamics model for accumulation of helium in tungsten under helium ions and neutron irradiation, Commun. Comput. Phys. 11 (2012) 1547–1568, https://doi.org/10.4208/cicp.030311.090611a.
[58] Z. Zhao, Y. Li, C. Zhang, G. Pan, P. Tang, Z. Zeng, Effect of grain size on the behavior of hydrogen/helium retention in tungsten: a cluster dynamics modeling, Nucl. Fusion 57 (2017), 086020, https://doi.org/10.1088/1741-4326/aa7640.
[59] E.V. Kornelsen, The interaction of injected helium with lattice defects in a tungsten crystal, Radiat. Eff. 13 (3–4) (1972) 227–236, https://doi.org/10.1080/00337577208231184.
[60] Y.G. Li, W.H. Zhou, L.F. Huang, Z. Zeng, X. Ju, Cluster dynamics modeling of accumulation and diffusion of helium in neutron irradiated tungsten, J. Nucl. Mater. 431 (2012) 26–32, https://doi.org/10.1016/j.jnucmat.2011.12.015.
[61] V.F. Sears, Kinetics of void growth in irradiated metals, J. Nucl. Mater. 39 (1) (1971) 18–26, https://doi.org/10.1016/0022-3115(71)90179-6.
[62] H. Wiedersich, On the theory of void formation during irradiation, Radiat. Eff. 12 (1–2) (1972) 111–125, https://doi.org/10.1080/00337577208231128.
[63] A.D. Brailsford, R. Bullough, The rate theory of swelling due to void growth in irradiated metals, J. Nucl. Mater. 44 (2) (1972) 121–135, https://doi.org/10.1016/0022-3115(72)90091-8.
[64] A.D. Brailsford, R. Bullough, M.R. Hayns, Point defect sink strengths and void-swelling, J. Nucl. Mater. 60 (3) (1976) 246–256, https://doi.org/10.1016/0022-3115(76)90139-2.
[65] J. Fikar, R. Schäublin, D.R. Mason, D. Nguyen-Manh, Nano-sized prismatic vacancy dislocation loops and vacancy clusters in tungsten, Nucl. Mater. Energy 16 (2018) 60–65, https://doi.org/10.1016/j.nme.2018.06.011.
[66] A. Hasegawa, M. Fukuda, T. Tanno, S. Nogami, Neutron irradiation behavior of tungsten, Mater. Trans. 54 (2013) 466–471, https://doi.org/10.2320/matertrans.MG201208.
[67] A. Hasegawa, M. Fukuda, K. Yabuuchi, S. Nogami, Neutron irradiation effects on the microstructural development of tungsten and tungsten alloys, J. Nucl. Mater. 471 (2016) 175–183, https://doi.org/10.1016/j.jnucmat.2015.10.047.
[68] W. Jäger, M. Wilkens, Formation of vacancy-type dislocation loops in tungsten bombarded by 60 kev au ions, Phys. Status Solidi 32 (1) (1975) 89–100, https://doi.org/10.1002/pssa.2210320109.
[69] D.R. Mason, X. Yi, M.A. Kirk, S.L. Dudarev, Elastic trapping of dislocation loops in cascades in ion-irradiated tungsten foils, J. Phys. Condens. Matter 26 (37) (2014), 375701, https://doi.org/10.1088/0953-8984/26/37/375701.
[70] O. El-Atwani, J.A. Hinks, G. Greaves, S. Gonderman, T. Qiu, M. Efe, J.P. Allain, In-situ tem observation of the response of ultrafine-and nanocrystalline-grained tungsten to extreme irradiation environments, Sci. Rep. 4 (2014) 4716, https://doi.org/10.1038/srep04716.
[71] F. Ferroni, X. Yi, K. Arakawa, S.P. Fitzgerald, P.D. Edmondson, S.G. Roberts, High temperature annealing of ion irradiated tungsten, Acta Mater. 90 (2015) 380–393, https://doi.org/10.1016/j.actamat.2015.01.067.
[72] O. El-Atwani, E. Esquivel, M. Efe, E. Aydogan, Y.Q. Wang, E. Martinez, S.A. Maloy, Loop and void damage during heavy ion irradiation on nanocrystalline and coarse grained tungsten: microstructure, effect of dpa rate, temperature, and grain size, Acta Mater. 149 (2018) 206–219, https://doi.org/10.1016/j.actamat.2018.02.035.
[73] H. Föll, M. Wilkens, A simple method for the analysis of dislocation loops by means of the inside-outside contrast on transmission electron micrographs, Phys. Status Solidi 31 (2) (1975) 519–524, https://doi.org/10.1002/pssa.2210310223.
[74] R.C. Rau, Vacancy dislocation loops in irradiated and annealed tungsten, Phil. Mag. 18 (155) (1968) 1079–1084, https://doi.org/10.1080/14786436808227526.
[75] Y. Watanabe, H. Iwakiri, N. Yoshida, K. Morishita, A. Kohyama, Formation of interstitial loops in tungsten under helium ion irradiation: rate theory modeling and experiment, Nucl. Instrum. Methods Phys. Res. Sect. B Beam Interact. Mater. Atoms 255 (2007) 32–36, https://doi.org/10.1016/j.nimb.2006.11.008.
[76] T. Faney, B.D. Wirth, Spatially dependent cluster dynamics modeling of microstructure evolution in low energy helium irradiated tungsten, Model. Simulat. Mater. Sci. Eng. 22 (2014), 065010, https://doi.org/10.1088/0965-0393/22/6/065010.
[77] D. Perez, L. Sandoval, S. Blondel, B.D. Wirth, B.P. Uberuaga, A.F. Voter, The mobility of small vacancy/helium complexes in tungsten and its impact on retention in fusion-relevant conditions, Sci. Rep. 7 (2017) 2522, https://doi.org/10.1038/s41598-017-02428-2.
[78] M. Jin, C. Permann, M.P. Short, Breaking the power law: multiscale simulations of self-ion irradiated tungsten, J. Nucl. Mater. 504 (33–40) (2018), https://doi.org/10.1016/j.jnucmat.2018.03.018.
[79] C.-C. Fu, F. Willaime, Interaction between helium and self-defects in α-iron from first principles, J. Nucl. Mater. 367 (2007) 244–250, https://doi.org/10.1016/j.jnucmat.2007.03.002.
[80] J. Marian, T.L. Hoang, Modeling fast neutron irradiation damage accumulation in tungsten, J. Nucl. Mater. 429 (2012) 293–297, https://doi.org/10.1016/j.jnucmat.2012.06.019.
[81] E. Gao, N.M. Ghoniem, A coupled rate theory-Monte Carlo model of helium bubble evolution in plasma-facing micro-engineered tungsten, J. Nucl. Mater. 509 (2018) 577–590, https://doi.org/10.1016/j.jnucmat.2018.04.051.
[82] J. Boisse, A. De Backer, C. Domain, C.S. Becquart, Modeling of the self trapping of helium and the trap mutation in tungsten using DFT and empirical potentials based on DFT, J. Mater. Res. 29 (2014) 2374–2386, https://doi.org/10.1557/jmr.2014.258.
[83] J. Boisse, C. Domain, C.S. Becquart, Modelling self trapping and trap mutation in tungsten using DFT and Molecular Dynamics with an empirical potential based on DFT, J. Nucl. Mater. 455 (1–3) (2014) 10–15, https://doi.org/10.1016/j.jnucmat.2014.02.031.
[84] C.S. Becquart, C. Domain, U. Sarkar, A. Debacker, M. Hou, Microstructural evolution of irradiated tungsten: ab initio parameterisation of an OKMC model, J. Nucl. Mater. 403 (75–88) (2010), https://doi.org/10.1016/j.jnucmat.2010.06.003.
[85] C.S. Becquart, M.F. Barthe, A. De Backer, Modelling radiation damage and he production in tungsten, Phys. Scripta 2011 (T145) (2011), https://doi.org/10.1088/0031-8949/2011/T145/014048, 014048.
[86] H.-B. Zhou, X. Ou, Y. Zhang, X. Shu, Y.-L. Liu, G.-H. Lu, Effect of carbon on helium trapping in tungsten: a first-principles investigation, J. Nucl. Mater. 440 (1–3) (2013) 338–343, https://doi.org/10.1016/j.jnucmat.2013.05.070.
[87] A. Dubinko, D. Terentyev, A. Bakaeva, K. Verbeken, M. Wirtz, M. Hernández-Mayoral, Evolution of plastic deformation in heavily deformed and recrystallized tungsten of iter specification studied by tem, Int. J. Refract. Metals Hard Mater. 66 (2017) 105–115, https://doi.org/10.1016/j.ijrmhm.2017.03.004.

[88] T.R. Waite, Theoretical treatment of the kinetics of diffusion-limited reactions, Phys. Rev. 107 (1957) 463, https://doi.org/10.1103/PhysRev.107.463.
[89] R. Bullough, M.R. Hayns, M.H. Wood, Sink strengths for thin film surfaces and grain boundaries, J. Nucl. Mater. 90 (1980) 44–59, https://doi.org/10.1016/0022-3115(80)90244-5.
[90] T. Ahlgren, K. Heinola, N. Juslin, A. Kuronen, Bond-order potential for point and extended defect simulations in tungsten, J. Appl. Phys. 107 (2010), 033516, https://doi.org/10.1063/1.3298466.
[91] P.A.T. Olsson, Semi-empirical atomistic study of point defect properties in bcc transition metals, Comput. Mater. Sci. 47 (2009) 135–145, https://doi.org/10.1016/j.commatsci.2009.06.025.
[92] J. Fikar, R. Schäublin, Atomistic simulations of nanometric dislocation loops in bcc tungsten, Nucl. Instrum. Methods Phys. Res. Sect. B Beam Interact. Mater. Atoms 267 (2009) 3218–3222, https://doi.org/10.1016/j.nimb.2009.06.075.
[93] N. Juslin, B.D. Wirth, Interatomic potentials for simulation of He bubble formation in W, J. Nucl. Mater. 432 (2013) 61–66, https://doi.org/10.1016/j.jnucmat.2012.07.023.
[94] T. Amino, K. Arakawa, H. Mori, Detection of one-dimensional migration of single self-interstitial atoms in tungsten using high-voltage electron microscopy, Sci. Rep. 6 (2016), 26099, https://doi.org/10.1038/srep26099.
[95] R.W. Balluffi, Vacancy defect mobilities and binding energies obtained from annealing studies, J. Nucl. Mater. 69 (1978) 240–263, https://doi.org/10.1016/0022-3115(78)90247-7.
[96] J.N. Mundy, S.T. Ockers, L.C. Smedskjaer, Vacancy migration enthalpy in tungsten at high temperatures, Philos. Mag. A 56 (1987) 851–860, https://doi.org/10.1080/01418618708204493.
[97] R.E. Stoller, G.R. Odette, A composite model of microstructural evolution in austenitic stainless steel under fast neutron irradiation. Radiation-Induced Changes in Microstructure: 13th International Symposium (Part I), ASTM International, 1987.
[98] R.E. Stoller, Modeling dislocation evolution in irradiated alloys, Metall. Trans. A 21 (1990) 1829–1837, https://doi.org/10.1007/BF02647229.
[99] M.G.D. Geers, M. Cottura, B. Appolaire, E.P. Busso, S. Forest, A. Villani, Coupled glide-climb diffusion-enhanced crystal plasticity, J. Mech. Phys. Solid. 70 (2014) 136–153, https://doi.org/10.1016/j.jmps.2014.05.007.
[100] J.ThM. de Hosson, A.W. Sleeswyk, L.M. Caspers, W. Van Heugten, A. Van Veen, The interaction of He with a 12 < 1 1 1 > { 1 1 0 } edge dislocation in W and Mo, Solid State Commun. 18 (1976) 479–482, https://doi.org/10.1016/0038-1098(76)90319-7.
[101] H.-B. Zhou, Y.-H. Li, G.-H. Lu, Modeling and simulation of helium behavior in tungsten: a first-principles investigation, Comput. Mater. Sci. 112 (2016) 487–491, https://doi.org/10.1016/j.commatsci.2015.09.019.
[102] X.-X. Wang, L.-L. Niu, S. Wang, Strong trapping and slow diffusion of helium in a tungsten grain boundary, J. Nucl. Mater. 487 (2017) 158–166, https://doi.org/10.1016/j.jnucmat.2017.02.010.
[103] W.-H. He, X. Gao, D. Wang, N. Gao, M.-H. Cui, L.-L. Pang, Z.-G. Wang, First-principles investigation of grain boundary morphology effects on helium solutions in tungsten, Comput. Mater. Sci. 148 (2018) 224–230, https://doi.org/10.1016/j.commatsci.2018.02.044.
[104] D.R. Olander, Fundamental Aspects of Nuclear Reactor Fuel Elements, TID26711-P1, 1976.
[105] N.M. Ghoniem, M.L. Takata, A rate theory of swelling induced by helium and displacement damage in fusion reactor structural materials, J. Nucl. Mater. 105 (1982) 276–292, https://doi.org/10.1016/0022-3115(82)90385-3.
[106] C. Dethloff, Modeling of Helium Bubble Nucleation and Growth in Neutron Irradiated RAFM Steels, vol. 6, KIT Scientific Publishing, 2014.
[107] LANL, Total neutron cross sections of the hydrogen and helium isotopes, Nucl. Phys. 12 (1959), https://doi.org/10.1016/0029-5582(59)90175-0.
[108] M.R. Gilbert, S.L. Dudarev, S. Zheng, L.W. Packer, J-Ch Sublet, An integrated model for materials in a fusion power plant: transmutation, gas production, and helium embrittlement under neutron irradiation, Nucl. Fusion 52 (2012), https://doi.org/10.1088/0029-5515/52/8/083019, 083019.
[109] G.S. Was, Fundamentals of Radiation Materials Science: Metals and Alloys, Springer, 2016.
[110] A.E. Sand, S.L. Dudarev, K. Nordlund, High-energy collision cascades in tungsten: dislocation loops structure and clustering scaling laws, EPL (Europhys. Lett.) 103 (2013), 46003, https://doi.org/10.1209/0295-5075/103/46003.
[111] X. Yi, A.E. Sand, D.R. Mason, M.A. Kirk, S.G. Roberts, K. Nordlund, S.L. Dudarev, Direct observation of size scaling and elastic interaction between nano-scale defects in collision cascades, EPL (Europhys. Lett.) 110 (2015), 36001, https://doi.org/10.1209/0295-5075/110/36001.
[112] W. Setyawan, G. Nandipati, K.J. Roche, H.L. Heinisch, B.D. Wirth, R.J. Kurtz, Displacement cascades and defects annealing in tungsten, part I: defect database from molecular dynamics simulations, J. Nucl. Mater. 462 (2015) 329–337, https://doi.org/10.1016/j.jnucmat.2014.12.056.
[113] D. Kaoumi, Microstructure Evolution of Nanocrystalline Metals under In-Situ Charged-Particle Irradiation in a Transmission Electron Microscope, PhD thesis, The Pennsylvania State University, 2007.
[114] G. Federici, et al., In-vessel tritium retention and removal in ITER, J. Nucl. Mater. 266 (1999) 14–29, https://doi.org/10.1016/S0022-3115(98)00876-9.
[115] D. Nishijima, M.Y. Ye, N. Ohno, S. Takamura, Formation mechanism of bubbles and holes on tungsten surface with low-energy and high-flux helium plasma irradiation in NAGDIS-II, J. Nucl. Mater. 329 (2004) 1029–1033, https://doi.org/10.1016/j.jnucmat.2004.04.129.
[116] Y. Minyou, Effects of low energy and high flux helium/hydrogen plasma irradiation on tungsten as plasma facing material, Plasma Sci. Technol. 7 (2005) 2828, https://doi.org/10.1088/1009-0630/7/3/010.
[117] K.D. Hammond, B.D. Wirth, Crystal orientation effects on helium ion depth distributions and adatom formation processes in plasma-facing tungsten, J. Appl. Phys. 116 (14) (2014), 143301, https://doi.org/10.1063/1.4897419.
[118] J.F. Ziegler, M.D. Ziegler, J.P. Biersack, SRIM-The stopping and range of ions in matter, Nucl. Instrum. Methods Phys. Res. Sect. B Beam Interact. Mater. Atoms 268 (2010) 1818–1823, https://doi.org/10.1016/j.nimb.2010.02.091, 2010.
[119] R.J. LeVeque, Finite Difference Methods for Ordinary and Partial Differential Equations: Steady-State and Time-dependent Problems, vol. 98, SIAM, 2007.
[120] S. Panayotis, T. Hirai, J.-M. Martinez, Thermo-mechanical Analysis of Chamfered and Non-chamfered Tungsten Monoblock, ITER organization, 2015 (Internal report).
[121] L. De-shun, X. Hui-zhong, W. Yan-sen, Z. Guo-qing, P. Shu-ming, Z. Peng-ji, X. Zhi-lei, Calculation of diffusion barriers for helium atom in metals, Acta Phys. Sin. 8 (1999) 746, https://doi.org/10.1088/1004-423X/8/10/004.
[122] A.C. Hindmarsh, P.N. Brown, K.E. Grant, S.L. Lee, R. Serban, D.E. Shumaker, C.S. Woodward, SUNDIALS: suite of nonlinear and differential/algebraic equation solvers, ACM Trans. Math Software 31 (2005) 363–396, https://doi.org/10.1145/1089014.1089020.
[123] A.A. Kohnert, B.D. Wirth, L. Capolungo, Modeling microstructural evolution in irradiated materials with cluster dynamics methods: a review, Comput. Mater. Sci. 149 (2018) 442–459, https://doi.org/10.1016/j.commatsci.2018.02.049.
[124] E. Lassner, W.D. Schubert, Tungsten: Properties, Chemistry, Technology of the Element, Alloys, and Chemical Compounds, 1999.
[125] Q. Xu, N. Yoshida, T. Yoshiie, Accumulation of helium in tungsten irradiated by helium and neutrons, J. Nucl. Mater. 367 (2007) 806–811, https://doi.org/10.1016/j.jnucmat.2007.03.078.